Development of an Electromagnetic Energy Harvester for Monitoring Wind Turbine Blades

Bryan Steven Joyce

Thesis submitted to the faculty of the
Virginia Polytechnic Institute and State University
in partial fulfillment of the requirements for the degree of

Master of Science
in
Mechanical Engineering

Daniel J. Inman, Chair
Mary E. Kasarda
Pablo A. Tarazaga

December 12, 2011
Blacksburg, Virginia

Keywords: energy harvesting, electromagnetic, wind turbine blades,
structural health monitoring

Development of an Electromagnetic Energy Harvester for Monitoring Wind Turbine Blades

Bryan Steven Joyce

ABSTRACT

Wind turbine blades experience tremendous stresses while in operation. Failure of a blade can damage other components or other wind turbines. This research focuses on developing an electromagnetic energy harvester for powering structural health monitoring (SHM) equipment inside a turbine blade. The harvester consists of a magnet inside a tube with coils outside the tube. The changing orientation of the blade causes the magnet to slide along the tube, inducing a voltage in the coils which in turn powers the SHM system. This thesis begins with a brief history of electromagnetic energy harvesting and energy harvesters in rotating environments. Next a model of the harvester is developed encompassing the motion of the magnet, the current in the electrical circuit, and the coupling between the mechanical and electrical domains. The nonlinear coupling factor is derived from Faraday's law of induction and from modeling the magnet as a magnetic dipole moment. Three experiments are performed to validate the model: a free fall test to verify the coupling factor expression, a rotating test to study the model with a load resistor circuit, and a capacitor charging test to examine the model with an energy storage circuit. The validated model is then examined under varying tube lengths and positions, varying coil sizes and positions, and variations in other parameters. Finally a sample harvester is presented that can power an SHM system inside a large scale wind turbine blade spinning up to 20 RPM and can produce up to 14.1 mW at 19 RPM.

Acknowledgments

First I would like to thank my advisor Dr. Daniel J. Inman. His diligence and his famous sense of humor has been a source of inspiration. I would also like to thank my committee members, Dr. Mary Kasarda and Dr. Pablo Tarazaga, for their support and guidance.

This research would not be possible without the assistance of Justin Farmer, lab manager at the Center for Intelligent Material Systems and Structures (CIMSS). I have greatly valued his help in setting up experiments, his input in discussing modeling and experimental results, and his friendly personality and positive outlook on life. I would like to extend my gratitude to program manager Beth Howell. CIMSS would not be complete without her dedication and hard work. Her wonderful personality has made CIMSS a terrific work environment. I would also like to thank Cathy Hill for helping me navigate through the graduate school program.

I am grateful for my colleagues at CIMSS. I would like to thank Dr. Steve Anton, Dr. Alper Erturk, Dr. Amin Karami, Mana Afshari, Jacob Dodson, Nick Thayer, Michael Okyen, Eric Baldrighi, Preston Pinto, Joseph Najem and all of my other friends at CIMSS for their help, their friendship, and their support.

Support for this research was provided by the US Department of Commerce, National Institute of Standards and Technology, Technology Innovation Program, Cooperative Agreement Number 70NANB9H9007.

Table of Contents

List of Figures

List of Tables

Nomenclature

a = radius of a ring inside the coil

$\hat{\mathbf{a}}$ = unit vector in the positive a-direction (outward from the coil)

$\bar{a}$ = mean radius of the coil

a_1 = inner radius of the coil

a_2 = outer radius of the coil

$\mathbf{B}$ = magnetic flux density field

B = magnitude of $\mathbf{B}$

B_a = component of $\mathbf{B}$ pointing in the a-direction

B_r = residual magnetic flux density of the permanent magnet

B_z = component of $\mathbf{B}$ pointing in the z-direction

C = capacitance

c = radial position of a ring inside the coil

c_1 = radial position of the bottom of the coil

c_2 = radial position of the top of the coil

D_w = wire diameter

dl = differential length of wire

$\mathbf{dl}$ = vector of differential length pointing tangentially to the wire

$d\mathrm{V}$ = differential volume element of the coil

E_C = energy stored on the capacitor

E_{load} = energy dissipated across the load resistor

e = distance from the axis of rotation to the center of mass of the rotor assembly

FF = fill factor of the coil

F_{em} = electromagnetic drag force

F_f = Coulomb friction force

F_p = applied force on the magnet opposing the force of friction

G = balance quality grade

g = acceleration due to gravity (9.81 m/s^2)

h = height of the coil

I = current flowing through the coil

I_C = current flowing through the capacitor

i = subscript designating a variable is evaluated at a discrete time t_i in the model algorithm

L_{coil} = inductance of the coil

l = tube length

l_w = length of wire composing the coil

M = mass of the magnet

M_{harv} = mass of the energy harvester

M_{rotor} = mass of the wind turbine rotor

M_{SHM} = mass of the SHM system

m = magnetic dipole moment

$\mathbf{m}$ = magnetic dipole moment vector

N = normal force

n = number of turns of wire

P_{load} = power dissipated across the load resistor

$\overline{P}_{load}$ = average power dissipated across the load resistor

q = charge stored on the capacitor

R_{coil} = electrical resistance of the coil

R_{load} = electrical resistance of the load resistor

r = radial position of the magnet

$\hat{\mathbf{r}}$ = unit vector in the positive r-direction

r_1 = minimum radial position of the magnet (radial position of the bottom of the tube)

r_2 = maximum radial position of the magnet (radial position of the top of the tube)

r_{SHM} = radial position of the SHM system's center of mass

T = total run time of an experiment or a numerical simulation

t = time

t' = dummy variable for time

V_{bridge} = voltage drop across the diode bridge

V_C = voltage across the capacitor

V_{coil} = volume of the coil

V_{load} = voltage across a load resistor

V_m = volume of the magnet

v = relative velocity between the magnet and the coil

$\mathbf{v}$ = relative velocity vector between the magnet and the coil

v_{RMS} = root-mean-square value of the magnet's radial velocity

z = distance from the magnet to a ring inside the coil

$\hat{\mathbf{z}}$ = unit vector in the positive z-direction

α = electromechanical coupling factor

β = angle used in coupling factor derivation

$\hat{\boldsymbol{\beta}}$ = unit vector in the positive β-direction (tangential to the wire)

Δt = size of time step in model algorithm

ε = voltage (or EMF) induced in the coil by the magnet

θ = angle between the tube and the vertically-upward position

$\hat{\boldsymbol{\theta}}$ = unit vector in the positive θ-direction

μ_0 = permeability of free space ($4\pi \times 10^{-7}$ H/m)

μ_k = kinetic coefficient of friction

μ_s = static coefficient of friction

ρ = electrical resistivity

ΣF_r = sum of the forces on the magnet in the r-direction

ΣF_θ = sum of the forces on the magnet in the θ-direction

Ω = rotation speed of the turbine

Ω_{peak} = peak speed

Ω^{v}_{peak} = velocity peak speed

Chapter 1 Introduction and Literature Review

This research examines an electromagnetic energy harvester for use inside a wind turbine blade. This chapter begins by discussing the motivation for this research. Next a brief overview of electromagnetic energy harvesting is given followed by a review of energy harvesters for use inside wind turbine blades and other rotating environments. An energy harvester design is proposed for powering a structural health monitoring system inside a turbine blade. Finally this chapter concludes with an outline of the research into this harvester design.

1.1 Research Motivation

Interest in renewable energy has grown over the past few decades. The renewable energy movement began to receive widespread attention during the energy crisis of the 1970s. Since then the alternative energy demand has been driven by public concern for cleaner energy and alternatives to fossil fuels [1]. Wind energy has emerged as a strong leader in the renewable energy field. Wind turbines are responsible for over 42,000 MW of the power generated in the U.S. Over 35% of this generating capacity was installed over the past four years [2].

However wind turbines have their drawbacks. Large scale wind turbines with power outputs over 1 MW can have blade lengths in excess of fifty meters [3, 4]. These long blades increase the swept area of the rotor which increases the amount of wind energy that can be captured by the blades. Consequently this increases the power output of the turbine. Wind turbine blades are made from a lightweight combination of balsa wood and fiberglass to reduce the weight of the rotor and to further increase power production [5]. These long composite

blades undergo cyclic loading while in operation, and thus fatigue and crack formation present safety concerns. Ice accumulation, lightning strikes, and bird and bat impacts can also harm the blades. Failure of a blade can damage other blades, internal components of the turbine, or other wind turbines [6]. Blade failure results in a loss of equipment and loss of revenue; a single blade for a large scale wind turbine can cost over $50,000 [7, 8]. Often turbines are located in remote areas such as mountainous regions or rough seas. This makes turbine inspection and maintenance difficult. In addition the tall heights of these wind turbines further complicate their upkeep. These factors create a desire to improve turbine safety and reliability without significantly reducing their performance or increasing their production costs [6].

One solution to this problem is to utilize a structural health monitoring (SHM) system to evaluate the structural integrity of the wind turbine blades while in operation. These systems detect damage to a structure through non-destructive methods such as impedance-based methods, acoustic emission, active thermography, ultrasonic inspection, and fiber-optic strain sensing [9]. Sensors placed along the length of the blade can detect that damage has occurred, determine the location of failure, evaluate the level of danger, and wirelessly transmit this information to a receiver unit on the turbine's nacelle. A SHM system inside a wind turbine blade offers multiple benefits. The autonomous system can monitor blades on turbines in remote areas and alert technicians before catastrophic failure occurs. Maintenance costs can be reduced as technicians do not need to inspect the blades as frequently. Because a damage detection system is in place, the blades can be designed with a lower factor of safety. This translates into lighter, more efficient wind turbine blades. Moreover, the knowledge gained from studying the blades while in service can be used to improve future blade designs [1].

The spinning rotor makes it difficult to power an SHM system inside a blade. Extracting power from the turbine's generator requires using slip rings to transfer current from the stationary nacelle to the spinning rotor. Using a power source inside the turbine blade avoids this problem and allows for a convenient SHM and power source system to be installed. Batteries could power the SHM equipment, however batteries have a limited lifespan and require regular replacement. A better alternative is to generate the required power using an energy harvesting system. An energy harvesting device could convert the rotation of the wind turbine into electrical energy. Such a system offers the possibility of powering a SHM device without the need of a battery.

Due to their size, weight, and cost, large scale wind turbines are of prime interest in using SHM equipment. This research focuses on producing power from the rotating blade of a large scale wind turbine. Wind turbines with power outputs over 1 MW typically operate at rotation speeds up to 20 RPM [3, 4, 10]. To reduce the added imbalance to the rotor, the harvester and SHM equipment should be placed as close to the center of rotation (toward the base of the blade) as possible. The power requirement of an SHM system can vary between 100 mW and 500 mW [11, 12].

1.2 Overview of Energy Harvesting

Energy harvesting or energy scavenging is the process of transforming ambient energy into useful electrical energy. The ambient energy could be the kinetic energy of a moving or vibrating structure, the radiant energy of sunlight, or the thermal energy of a warm object. An energy harvesting device captures what would otherwise be wasted energy from its environment

while minimally affecting the characteristics of its host structure or its surroundings. The advent of modern electronics brought about an interest in energy harvesting. As technology progressed, smaller electronic devices with lower power demands became available [13]. It became possible to use a small energy harvester to power these electronic devices using only ambient energy. Energy harvesters have been used in applications such as rechargeable batteries, air pressure sensors in automobile tires, unmanned vehicles, embedded and implanted medical sensors, and structural health monitoring [14].

Several energy harvesting methods exist including thermoelectric, photovoltaic, electromagnetic, piezoelectric, magnetostrictive, and electrostatic. Thermoelectric energy harvesters convert heat into electrical energy, while photovoltaic energy harvesters produce electrical energy from solar radiation [15]. There are several energy harvesting methods that convert mechanical energy into electrical energy. Electromagnetic energy harvesters (also called induction energy harvesters) use the motion of a permanent magnet to induce a voltage across the terminals of a coil of wire. This voltage is used to energize an electrical circuit. A piezoelectric material will produce an electric field and consequently a voltage when deformed under an applied stress [16]. Similarly, a magnetostrictive material will produce a magnetic field when deformed. If there is a conductive coil nearby, this magnetic field will generate a voltage across the coil [17]. Electrostatic energy harvesters use the vibration of a host structure to vary the capacitance of an initially charged capacitor. This variable capacitor acts like a current source that can power an electrical circuit [18]. The research presented here will focus on an electromagnetic energy harvester to produce electrical power from the rotation of a wind turbine blade.

1.3 Brief Overview of Electromagnetic Energy Harvesting

Nineteenth century scientists such as Hans Oersted, Joseph Henry, Michael Faraday, James Maxwell, and Heinrich Hertz pioneered the early work in electromagnetism. The famous Maxwell equations describe the interplay between magnetic and electric fields. One of these equations, Faraday's law of induction, describes how a time varying magnetic field will induce an electric field. Thus a permanent magnet moving relative to a conductive coil of wire will induce an electric potential (i.e. a voltage) across the terminals of the coil. Faraday was the first to develop an electric generator based on this principle [19]. Today electrical generators have widespread use in power generation systems such as fossil fuels, nuclear power, hydroelectric power, and wind turbines. Summarizing the last century of development in electromagnetism and electrical generators would be a daunting task. Instead this section will focus on an overview of induction energy harvesters, i.e. electromagnetic generators that produce power from ambient energy. Arnold [20] and Mitcheson [21, 22] provide comprehensive reviews of some electromagnetic energy harvesting techniques.

Inductive energy harvesters can be categorized by how they achieve a relative velocity between the coil and the magnet. Linear harvesters feature the magnet moving along a straight line relative to the coil. Rotational harvesters use magnets mounted on a spinning rotor with stationary coils mounted around the rotor. Pendulum harvesters feature the magnet on a pendulum moving relative to a stationary coil. Beam-based harvesters attach either a magnet or a coil to an elastic beam.

In 1995 and 1996 Williams and Yates [23, 24] modeled a simple linear energy harvester. The device consisted of a proof mass connected to a rigid frame using a spring. The

electromagnetic energy harvester was modeled as a dashpot which exerted a force on the mass that was directly proportional to the relative velocity between the mass and the frame. As the rigid frame oscillated, some of the mechanical energy of the moving proof mass was transferred through the harvester to a load resistor. Williams and Yates concluded that increasing the natural frequency or the deflection of the proof mass would increase the power output of the device to the load resistor. Their calculations showed that this harvester design with a volume of 25 mm^3 could produce 0.1 mW at 330 Hz from an assumed deflection of 50 μm. Williams *et al.* [25] constructed a linear micro-generator based on this design. The 25 mm^3 device consisted of a permanent magnet attached to a polyimide membrane suspended above a gold coil. The device produced up to 0.3 μW at 4.4 kHz from a 0.5 μm displacement.

In 1998 Amirtharajah and Chandrakasan [13] demonstrated that a digital signal processing (DSP) chip could be powered by the vibrations of a person walking. The DSP chip featured a subband FIR filter and electrical components to condition the voltage from an electromagnetic energy harvester. Their harvester used the same mass and spring system as described by Williams and Yates. Here a coil was mounted on a moving mass and a permanent magnet was mounted on the housing of the device. A prototype of their design produced 400 μW at 2 Hz from a 2 cm displacement. This was enough to meet the 18 μW power requirement of the DSP chip.

Zuo *et al.* [26] examined a linear electromagnetic energy harvester for vehicle suspensions. The regenerative shock absorber captured vibrations caused by road irregularities and vehicle accelerations and decelerations. The shock absorber was able to generate 16 W to 64 W from a RMS suspension velocity between 0.25 m/s and 0.5 m/s. Other researchers have examined linear generators for capturing the energy of ocean waves. These devices consist of a

buoy floating on the ocean surface attached by a cable to a sliding rod inside a generator on the seabed. As a wave passes, the vertical motion of the buoy pulls on a cable and moves the rod. Magnets mounted on the rod induce a voltage in the coils of the generator. Prudell and Brekken [27] examined a 1 kW generator, while Danielsson [28] modeled a 10 kW generator. Polinder *et al*. [29] estimated the annual energy output from a pilot plant of these generators to be 1.64 GWh.

Several researchers have studied rotational energy harvesters. Typically these harvesters require a mechanism to convert the linear motion of a vibrating structure into a rotational motion to drive the device. Rotational energy harvesters are not limited in displacement like linear harvesters, and this allows for larger power densities. However rotational generators typically operate at higher frequencies than linear generators [20]. An early electromagnetic energy harvester is the Seiko Kinetic self-powered wristwatch, first introduced at the 1986 Basel Fair [30]. The motion of the wearer turned an eccentric mass on the rotor of a small electric generator. There was no need for the user to wind the mainspring of the watch or replace a battery. Yeatman [31] studied the maximum power density of rotating and gyroscopic energy harvesters. His work concluded that rotational devices can achieve higher power densities than linear energy harvesters, but they require low parasitic damping. Furthermore if a torsion spring is used to connect the rotating mass to a rigid frame, then the spring must have a large angular range. Trimble *et al.* [32] examined a simple generator consisting of a rotating mass suspended by a torsion spring. Magnets attached to the rotating mass moved relative to coils mounted on the rigid housing. The 80 cm^3 prototype device was able to produce over 200 mW at a resonance frequency of 16 Hz and an angular acceleration of 150 rad/s^2.

Pendulum-based induction harvesters allow for rotational motion to be achieved through linear vibrations. Spreemann *et al.* [33] studied an energy harvester which featured magnets attached to an eccentric mass swinging near a set of coils. The 1.3 cm^3 device produced 2 mW at 60 Hz to 11 mW at 140 Hz with 0.2 mm vibration amplitude. A pendulum-based harvester design can also produce power when placed on a rotating structure. The next section will discuss other pendulum harvester designs.

Another electromagnetic harvester design is to attach either a magnet or a coil to an elastic beam. El-hami *et al.* [34] examined a micro-scale harvester consisting of a U-shaped bracket and magnet assembly mounted on a cantilever beam. A coil mounted to a stationary frame was positioned between the oscillating magnets on the bracket. The 240 mm^3 device produced 0.53 mW at a resonance frequency of 322 Hz from a 25 μm excitation amplitude. Yang *et al.* [35] examined a design using three magnets attached to an elastic beam that was clamped at both ends. The device captured energy at the first three natural frequencies of the beam: 369 Hz, 938 Hz, and 1184 Hz. The device was able to produce 3.2 μW at the second natural frequency from a 14 μm excitation amplitude. The use of an elastic beam also offers the potential to combine electromagnetic and piezoelectric energy harvesting methods. Challa [36] examined a piezoelectric cantilever beam with a magnet for a tip mass. The 35 cm^3 device generated a total of 332 μW from both energy harvesting methods at a resonant frequency of 21.6 Hz. Yang *et al.* [37] studied a 222 mm^3 cantilever harvester that generated a combined 176 μW at 310 Hz under a 2.5 g acceleration.

1.4 Energy Harvesters in Rotating Environments

There has been some interest in placing energy harvesters in rotating environments. A research group from Los Alamos studied energy harvesters inside wind turbine blades [38]. The project explored combining piezoelectric, thermoelectric, and photovoltaic energy harvesting methods to power an SHM device. Electromagnetic energy harvesting was not examined. The photovoltaic cell would be mounted on the outside of the blade, the thermoelectric generator would be integrated into the blade, and the piezoelectric harvester could be placed inside the blade. The power output from a 140 cm^2 photovoltaic cell was 235 mW (a power density of 1.67 mW/cm^2). From a temperature gradient of 10 °C, a thermoelectric harvester was able to produce 0.1 mW. Several piezoelectric harvester designs were tested to produce energy from the rotation of the blades. Each piezoelectric harvester was placed on a shaker and driven at its first natural frequency. A cantilever beam with a tip mass was able to charge a 1 mF capacitor to 3.5 V (6.1 mJ of energy) after 90 seconds. However the first natural frequency of this beam was 69 Hz. This frequency was above the maximum expected frequency in large scale turbines of 20 RPM (1/3 Hz). An L-shaped harvester presented a lower first natural frequency of 2.7 Hz. However this harvester was only able to charge the 1 mF capacitor to 1.0 V (0.5 mJ of energy).

Conrad [39] explored the concept of placing an electromagnetic energy harvester inside the rotating propeller of a large ship. This work examined several energy harvesters including a simple linear generator, a pendulum harvester, and a double pendulum harvester. The final design was a slider augmented pendulum. This design used a magnet on a pendulum with a rigid link connecting the magnet to a slider mass. The natural frequency of the device could be adjusted by changing the length of the rigid link or changing the slider mass. The harvester

placed one meter from the center of rotation produced over 80 mW to a 48 Ω load resistor at 150 RPM.

Toh *et al*. [40, 41, 42] examined a rotational generator placed on a spinning machine. The generator was position on the rotating machine with its shaft parallel to the axis of rotation of the host machine. An imbalanced mass was placed on the generator's rotor. As the host machine turned, the interplay between the force of gravity and centrifugal effects on the imbalanced mass spun the rotor and generated electricity. The device placed 1.5 cm from the center of rotation produced about 10 mW for a rotation speed of 240 RPM. Wang *et al*. [43] investigated a pendulum-type electromagnetic energy harvester mounted on a rotating wheel. The harvester used three magnets on an adjustable linkage. Changing the length of the linkage changed the natural frequency of the device to better suit the rotation rate of the wheel. The harvester produced a few milliwatts over a range between 200 RPM and 350 RPM.

Researchers have also examined energy harvesters inside automobile tires. Manla *et al*. [44] studied a piezoelectric generator to power tire pressure sensors. The design consisted of a ball bearing inside a tube that was positioned inside a tire. A pulley system would keep the tube in a horizontal position as the tire rotated. While the tire is rotating, the ball bearing would impact piezoelectric devices at the ends of the tube and generate electrical power. A prototype device produced 12 μW at 200 RPM. Other researchers examined using piezoelectric patches mounted to the tire wall. The deformation of the tire would strain the patch and generate a voltage. Hu *et al.* [45] was able to produce 70 μW/cm^3 from such a device.

Others have investigated piezoelectric beams mounted on rotating machinery. Khamenifar *et al.* [46] developed a cantilever beam with a tip mass for application on rotating devices. The beam was mounted with its base fixed to the host device and the length of the beam

pointed away from the center of rotation. Their harvester was able to produce 7.7 mW at a resonance frequency of 22 Hz. Gu and Livermore [47] examined a similar cantilever beam with a tip mass. Their analytical and experimental results demonstrated that the harvester had a limited self-tuning capability. The centrifugal effects on the beam varied the tension in beam with changing rotation speeds. This shifting tension altered the natural frequencies of the beam. For a range of input rotation speeds, the first natural frequency remained close to the driving frequency, and thus the device was kept close to resonance over a range of driving frequencies. The center of this frequency range was determined by the beam's dimensions and the distance from the beam to the center of rotation. For their harvester, their root of the beam was 6.9 cm from the center of rotation, and the driving frequencies were varied from 6.2 Hz to 16.2 Hz. The driving frequency and resonance frequency matched at 13.2 Hz and differed by a maximum of 0.5 Hz at 6.2 Hz. The harvester produced about 0.7 mW at 13.2 Hz.

1.5 Overview of the Energy Harvester Design

This research examines the use of a linear induction energy harvester to capture energy from the rotation of a wind turbine blade. Figure 1.1a shows a schematic of the proposed energy harvester design. The harvester consists of a tube with a coil on the outside and a magnet on the inside. The final design of the energy harvester features multiple coils along the tube. Figure 1.1b shows several harvesters inside the blades of a wind turbine. The harvesters are shown near the base of the blade to reduce the potential added imbalance to the rotor. As the rotor turns, the changing orientation of the blade causes the magnet to slide along the tube. The motion of the magnet induces a voltage across the terminals of the coil. The coil would be

connected to an energy storage circuit to store the generated energy for later use by the SHM system. The falling magnet can achieve high instantaneous velocities and thus large induced voltages even at low rotation speeds. The harvester's location inside the blade will not affect the airflow around the blades. The harvester's single moving part (the sliding magnet) helps to ensure the reliability of the device. Because this harvester is intended to function inside a large scale wind turbine, the harvester must be capable of producing power from rotation speeds up to 20 RPM.

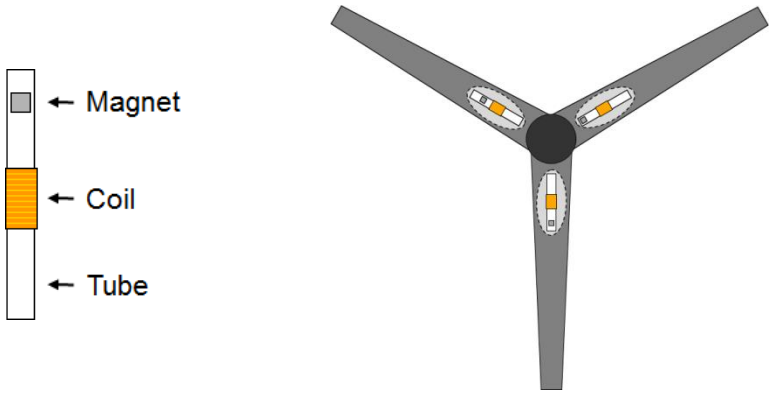

(a) (b)

Figure 1.1. (a) Diagram of the energy harvester assembly.
(b) Energy harvesters placed inside the blades of a wind turbine.

1.6 Research Outline

This thesis will detail the development of a linear induction energy harvester to power an SHM system inside a wind turbine blade. Chapter 2 focuses on the derivation of the energy harvester model. The harvester model consists of the mechanics of the magnet, the equations of the electrical circuit, and the coupling expression relating the motion of the magnet and the

current in the circuit. Chapter 3 examines the results of three tests used to validate the energy harvester model. A free fall test determines the validity of the electromechanical coupling factor. A rotating test compares the power output from a prototype harvester to predictions from the model. A capacitor charging test shows the prototype harvester can generate and store electrical energy. Chapter 4 examines the use of this energy harvester inside a full scale wind turbine blade and explores the performance of the harvester under varying tube lengths, tube positions, coil sizes, coil positions, and other parameters. A sample harvester is presented that can generate power over the range of expected operating speeds of a large scale wind turbine. Finally Chapter 5 summarizes the major results from this research, discusses how this work relates and contributes to other applications, and presents some prospects for future research.

Chapter 2 Derivation of the Energy Harvester Model

This chapter focuses on the mathematical model of the energy harvester. The model can be broken into three parts. The first part is the mechanics governing the motion of the magnet. The second part is the electromechanical coupling between the motion of the magnet and the current in the coil. The third part is the analysis of the electrical circuit. The equations from the three parts of the energy harvester model are solved using a MATLAB numerical solver. This chapter derives the equations behind the model and discusses the algorithm developed to solve these equations.

2.1 Mechanics

The first step in deriving the harvester model is to describe the motion of the magnet. The equation of motion can be found through Newton's second law of motion, however the ends of the tube and friction from the tube wall complicate the dynamics of the magnet.

2.1.1 Equation of Motion

Figure 2.1a shows a schematic of the harvester inside a wind turbine blade. The blade spins at a rotation rate Ω, and the radial position of the magnet (the distance from the center of the hub to the magnet) is r. The free body diagram in Figure 2.1b shows the magnet and the forces acting upon it. The angle between the tube and the vertically-upward position is θ. Here θ is taken to be positive in the clockwise direction. The time derivative of this angle is the

rotation speed of the rotor (i.e. $\dot{\theta} = \Omega$). The unit vector $\hat{\mathbf{r}}$ points in the positive *r*-direction, and the unit vector $\hat{\boldsymbol{\theta}}$ points in the positive θ-direction. The mass of the magnet is *M*, and the acceleration due to gravity is *g*. The walls of the tube provide a normal force (*N*) perpendicular to the side of the magnet and a friction force (F_f) pointing against the direction of motion. An electromagnetic drag force (F_{em}) occurs due to interaction between the magnetic field of the moving magnet and the magnetic field of the current-carrying coil.

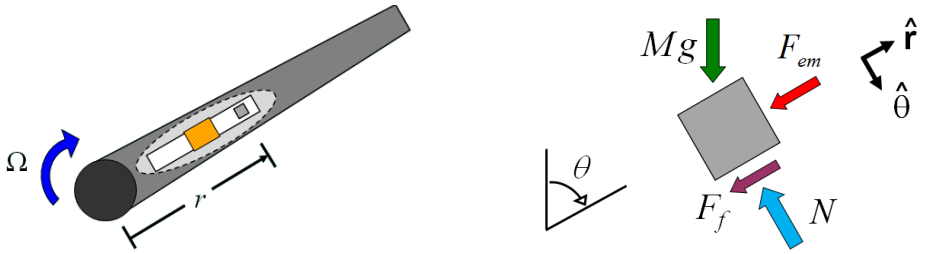

(a) (b)

Figure 2.1. (a) Schematic of the energy harvester inside a wind turbine blade. (b) Free body diagram of the magnet.

Newton's second law of motion can be applied to the magnet by setting the sum of the forces acting on the magnet in the *r*-direction equal to the mass of the magnet times its radial acceleration. This produces

$$\sum F_r = M\left(\ddot{r} - r\Omega^2\right), \tag{2.1}$$

$$-Mg\cos(\theta) - F_{em} - F_f = M\left(\ddot{r} - r\Omega^2\right), \tag{2.2}$$

where Ω is in radians per second. After rearranging terms, this equation becomes

$$M\ddot{r} - M\Omega^2 r + F_f + F_{em} = -Mg\cos(\theta). \tag{2.3}$$

The centrifugal term $M\Omega^2 r$ causes the above equation to be unstable. This instability is countered by the physical ends of the tube (see Section 2.1.3).

The electromagnetic drag force is related to the current in the coil by an electromechanical coupling factor (α). Section 2.2 discusses the coupling factor and provides a derivation. The coupling factor gives the electromagnetic drag force in terms of the current in the coil (I) as

$$F_{em} = \alpha(r) I \,, \tag{2.4}$$

where it is noted that the coupling factor depends on the radial position of the magnet (r). The final form of the equation of motion is

$$M\ddot{r} - M\Omega^2 r + F_f + \alpha(r) I = -Mg\cos(\theta) \,. \tag{2.5}$$

2.1.2 Coulomb Friction

Next the friction force needs to be evaluated. The friction between the magnet and the walls of the tube is modeled as Coulomb friction (also known as dry friction). To illustrate how Coulomb friction works, Figure 2.2 shows a block on a rough, flat surface with an applied force (F_p) pushing the block to the right. A friction force (F_f) opposes the block's intended motion. When the block is at rest, equilibrium dictates that the friction force must equal the applied force, namely

$$F_f = F_p \,. \tag{2.6}$$

The block will remain at rest as long as the applied force satisfies the inequality

$$F_p \le \mu_s N \,, \tag{2.7}$$

where μ_s is the static coefficient of friction and N is the normal force on the magnet from the contact surface. The normal force acts perpendicular to the contact surface. If the inequality is not satisfied, then the block will begin to move. The friction force on the moving block is

$$F_f = \mu_k N, \tag{2.8}$$

where μ_k is the kinetic coefficient of friction. Note that the friction force opposes the direction of the block's motion. The two coefficients of friction are dependent on the two materials in contact, and they must be experimentally determined.

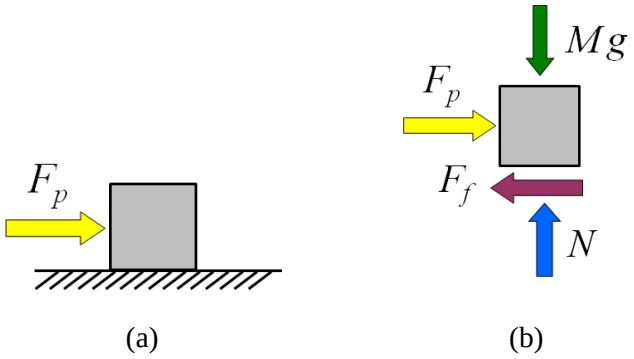

Figure 2.2. (a) Block on a rough surface. (b) Free body diagram of the block.

The magnet inside the harvester will experience Coulomb friction. The cylindrical tube wall can be in contact with any side of the magnet. The magnet will not slide along the tube ($\dot{r} = 0$) if the sum of the applied forces in the radial direction (F_p) satisfies the inequality

$$\left|F_p\right| \le \mu_s \left|N\right|. \tag{2.9}$$

Here absolute value signs are required. A negative value for the normal force would indicate the tube is in contact with the opposite side of the magnet. However, regardless of which side is in contact with the tube, the friction force must still oppose the motion of the magnet. F_p is found through examining the equation of motion. When the static friction force holds the magnet in

place relative to the tube wall, $\dot{r}$ and $\ddot{r}$ are zero and the friction force (F_f) equals the sum of the applied forces (F_p). Using this information and applying Newton's second law in the *r*-direction results in

$$-Mg\cos(\theta) - F_{em} - (F_p) = M\left((0) - r\Omega^2\right), \tag{2.10}$$

$$F_p = Mr\Omega^2 - Mg\cos(\theta) - F_{em}. \tag{2.11}$$

When the magnet is held in place by friction, the equation of motion does not apply because $\dot{r}$ and $\ddot{r}$ are zero. However when the above inequality is not satisfied for the magnet at rest, the magnet will begin to move and the equation of motion is applicable. In this case, the friction force on the magnet is

$$F_f = \mu_k |N| \operatorname{sgn}(\dot{r}), \tag{2.12}$$

where sgn is the signum function, defined as

$$\operatorname{sgn}(\dot{r}) = \begin{cases} 1 & \text{if } \dot{r} > 0 \\ 0 & \text{if } \dot{r} = 0 \\ -1 & \text{if } \dot{r} < 0 \end{cases}. \tag{2.13}$$

The use of the signum function ensures the friction force always opposes the motion of the magnet. From Figure 2.1b, Newton's second law of motion in the θ-direction gives

$$\sum F_\theta = Mg\sin(\theta) - N = M\left(r\dot{\Omega} + 2\dot{r}\Omega\right). \tag{2.14}$$

Thus the normal force is

$$N = M\left(g\sin(\theta) - r\dot{\Omega} - 2\dot{r}\Omega\right). \tag{2.15}$$

This expression for the normal force holds regardless of whether the magnet is moving relative to the tube wall or it is stationary.

2.1.3 End Conditions

In addition to the equation of motion, there are necessary kinematic constraints on the motion of the magnet imposed by the ends of the tube. Figure 2.3 shows the harvester inside a wind turbine blade. The figure indicates the radial position of the bottom of the tube (r_1) and the radial position of the top of the tube (r_2). The magnet cannot travel through the ends of the tube. Thus the radial position of the magnet is bound between r_1 and r_2. At the bottom of the tube, the radial velocity cannot be negative. At the top of the tube, the radial velocity cannot be positive. This is summarized as

$$\dot{r} \geq 0 \text{ if } r = r_1 \quad \text{and} \quad \dot{r} \leq 0 \text{ if } r = r_2 \tag{2.16}$$

Without these end conditions, the equation of motion is unstable, and the model would show the radial position of the magnet (r) increasing without bound. The ends of the tube prevent this instability and allow the magnet to oscillate inside the tube.

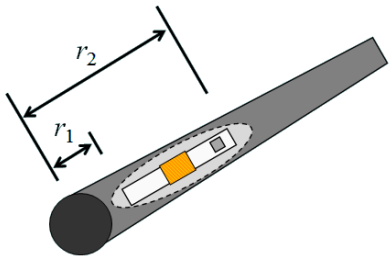

Figure 2.3. Schematic of the harvester showing the tube ends r_1 and r_2.

2.2 Electromechanical Coupling

Next an analytical expression was developed for the electromechanical coupling factor. One can define the coupling factor (α) through the equation

$$\varepsilon = \alpha(r)\,\dot{r}\,, \tag{2.17}$$

where ε is the induced voltage in the coil and $\dot{r}$ is the radial velocity of the magnet. It is noted that α is a function of the radial position of the magnet. Through the conservation of energy, the power into the electrical circuit is the power lost from the magnet due to the electromagnetic drag force, i.e.

$$\varepsilon\, I = F_{em}\,\dot{r}\,, \tag{2.18}$$

where I is the current in the coil [48]. Therefore the coupling factor must also relate the electromagnetic drag force to the current in the coil, namely

$$F_{em} = \alpha(r)\, I\,. \tag{2.19}$$

To find this coupling factor, one can start by examining how the induced voltage in the coil is related to the velocity of the magnet. From Faraday's law of induction, the induced voltage (also called an electromotive force or EMF) in a coil moving through a magnetic field is

$$\varepsilon = \oint_{l_w} (\mathbf{v}\times\mathbf{B})\cdot\mathbf{dl}\,, \tag{2.20}$$

where l_w is the length of wire composing the coil, **v** is relative velocity between the magnet and the coil, **B** is the magnetic flux density field of the magnet, and **dl** is a vector of differential length pointing tangentially to the wire. Figure 2.4 shows a ring of the coil, a permanent magnet, and the coordinates used to describe the magnetic field around the magnet. In this diagram, the ring is moving downward with a velocity v toward the stationary magnet (because the induced

voltage depends on the relative velocity, this is equivalent to the magnet moving upward with a velocity v toward a stationary ring). The magnet is drawn with a magnetic dipole moment vector **m** pointing toward the magnetic north of the magnet (this vector will be used later). The radius of the ring is a, and the distance from the top of the magnet to the plane containing the ring is z. The angle β is used later in an integration step; the reference axis is arbitrary due to the symmetry of the ring-magnet system. The unit vectors $\hat{\mathbf{z}}$, $\hat{\mathbf{a}}$, and $\hat{\boldsymbol{\beta}}$ point in the positive z-, a-, and β-directions, respectively. Figure 2.4 also indicates the velocity vector, the magnetic flux density vectors, and the differential length vector at a point on the ring. Due to the symmetry of the cylindrical magnet, the flux density field only has components in the a-direction (B_a) and z-direction (B_z).

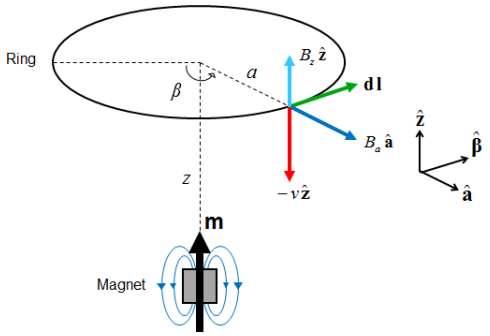

Figure 2.4. Ring moving toward a magnet.

Using Figure 2.4, the expression for the induced voltage becomes

$$\varepsilon = \oint_{l_w} [(-v\,\hat{\mathbf{z}}) \times (B_a\,\hat{\mathbf{a}} + B_z\,\hat{\mathbf{z}})] \cdot (dl\,\hat{\boldsymbol{\beta}}), \tag{2.21}$$

$$\varepsilon = -v \oint_{l_w} B_a\, dl\,. \tag{2.22}$$

Next a coordinate transform can be used to convert this expression into coordinates more useful for the harvester model. Figure 2.5 shows the new variables r and c along with several coil

parameters. The ring from Figure 2.4 is highlighted inside the coil. The inner radius of the coil is a_1, the outer radius is a_2, the radial position of the bottom of the coil is c_1, and the radial position of the top of the coil is c_2. The height of the coil (h) is the difference between the top and bottom radial positions (c_2 - c_1).

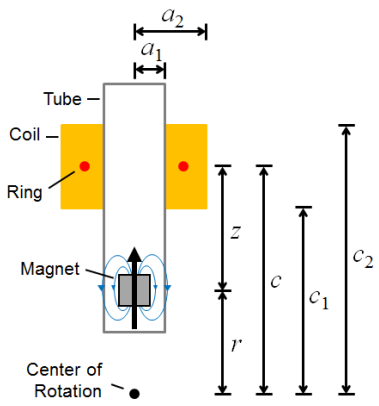

Figure 2.5. Diagram showing the relationship between the distances z, r, and c.

From Figure 2.5, the new variables r and c are related to z through the equation

$$z = c - r\,. \tag{2.23}$$

For the harvester, the ring is stationary and the magnet is in motion. Because the ring is stationary ($\dot{c} = 0$), the relative velocity v in terms of z and r is

$$v = \dot{z} = -\dot{r}\,. \tag{2.24}$$

Using this coordinate transformation, the expression for the induced voltage becomes

$$\varepsilon = \dot{r} \oint_{l_w} B_a \, dl\,. \tag{2.25}$$

From this and the definition of the electromechanical coupling factor, one can see that

$$\alpha(r) = \frac{\varepsilon}{\dot{r}} = \oint_{l_w} B_a \; dl\,. \tag{2.26}$$

The magnetic flux density and consequently the above integral depend on the separation distance between the magnet and the coil. Therefore α is a function of the position of the magnet (r). It should be noted that once the harvester begins to rotate, the relative velocity (v) between a ring in the coil and the magnet would have a component in the θ-direction due to the rotation of the tube and the distance between the magnet and the coil. However this component of the velocity is eliminated in the integration over the length of the wire, and therefore it can be ignored in determining the coupling factor.

From here there are multiple approaches to determining the coupling factor. Often researchers have treated the magnetic flux density as uniform over the coil volume and constant over the magnet's entire range of motion [21, 24, 49]. These assumptions lead to a coupling factor of

$$\alpha = Bl_w \tag{2.27}$$

where B is the magnitude of the magnetic flux density of the magnet. This approach simplifies analysis of the energy harvester. However a constant flux density assumption is not permissible here due to the large amplitude of motion of the magnet and the resulting large variation in the magnetic flux density at the coil. Therefore this harvester needs a coupling factor expression which depends on the position of the magnet. Some researchers have experimentally determined the coupling factor as a function of the magnet's position [39, 50]. This approach is useful for energy harvesters with difficult geometries. However an experimental technique does not give information about how changing the harvester's geometry or the coil's dimensions affect the coupling factor. A designer would need to conduct a new experiment for each new harvester configuration. Some sources have evaluated the coupling factor integral by expressing the magnetic flux density field using elliptic integrals and performing numerical integrations

[51, 52]. Other authors have modeled the magnet and coil using a finite element approach to evaluate the coupling factor integral [26, 53]. These approaches yield unnecessarily complex models which are computationally more difficult to include in the energy harvester model.

Here the approach is to evaluate the coupling factor expression analytically. An analytical expression can be evaluated quickly inside a numerical code and can be studied easily. The procedure here yields a nonlinear coupling factor similar to the one produced by Sneller and Mann [54]. First one can rewrite the coupling factor expression as

$$\alpha(r) = \oint_{l_w} B_a \, dl = \left(\frac{1}{l_w} \oint_{l_w} B_a \, dl \right) l_w . \tag{2.28}$$

One can see that the term in parentheses is the average of B_a over the length of the wire inside the coil. If the coil is tightly wound, then this average can be approximated as the average of B_a over the volume of the coil, i.e.

$$\alpha(r) = \left(\frac{1}{l_w} \oint_{l_w} B_a \, dl \right) l_w = \left(\frac{1}{\mathrm{V}_{coil}} \int_{\mathrm{V}_{coil}} B_a \, d\,\mathrm{V} \right) l_w . \tag{2.29}$$

where V_{coil} is the volume of the coil and $d\,\mathrm{V}$ is an infinitesimal volume element, which in cylindrical coordinates is

$$d\,\mathrm{V} = a \, da \, dc \, d\beta . \tag{2.30}$$

Next an expression for B_a is needed. An effective technique to model a permanent magnet is to treat the magnet as a magnetic dipole, i.e. two magnetic monopoles separated by a small distance [54, 55]. A magnetic dipole is characterized by a magnetic dipole moment vector **m** which indicates the orientation and the strength of the magnetic field. For a magnetic dipole, the component of the magnetic flux density field in the *a*-direction is

$$B_a = \frac{3\mu_0}{4\pi} m \frac{a\,z}{\left(a^2 + z^2\right)^{5/2}} , \tag{2.31}$$

where m is the magnitude of the vector **m** and μ_0 is the permeability of free space ($4\pi \times 10^{-7}$ H/m). This expression in terms of r and c is

$$B_a = \frac{3\mu_0}{4\pi} m \frac{a(c-r)}{\left(a^2 + (c-r)^2\right)^{5/2}} . \tag{2.32}$$

Thus the coupling factor becomes

$$\alpha(r) = \int_0^{2\pi} \int_{c_1}^{c_2} \int_{a_1}^{a_2} \frac{3\mu_0}{4\pi} m \frac{a(c-r)}{\left(a^2 + (c-r)^2\right)^{5/2}} \, (a \, da \, dc \, d\beta) . \tag{2.33}$$

Performing the integrations, one arrives at the final expression for the coupling factor,

$$\alpha(r) = \frac{1}{2} \frac{\mu_0 m l_w}{V_{coil}} \left\{ \frac{a}{\sqrt{a^2 + (r-c)^2}} - \ln\left(\sqrt{a^2 + (r-c)^2} + a\right) \right\} \Big|_{c=c_1}^{c_2} \Big|_{a=a_1}^{a_2} . \tag{2.34}$$

The two evaluation bars on the right side of the expression appear from the integrations over the coil volume. This final form of the coupling factor approximates the relationship between the motion of the magnet and the current in the coil, and it can be easily incorporated into the model of the energy harvester.

2.3 Electrical Circuit

Next the electrical circuit is analyzed. First a load resistance circuit is used to experimentally verify the model and to assess the performance of the harvester. This circuit dissipates the produced energy across a load resistor and it is not capable of storing energy. Next a basic energy storing circuit is examined that stores the generated energy inside a capacitor.

2.3.1 Load Resistance Circuit

Figure 2.6 shows the load resistor circuit. The coil is modeled as a series connection of an input voltage (ε) induced by the moving magnet, a coil inductance (L_{coil}), and a coil resistance (R_{coil}). A load resistor (R_{load}) is connected to the coil and completes the electrical circuit. When the magnet is moving and inducing a voltage, a current (I) flows through the circuit.

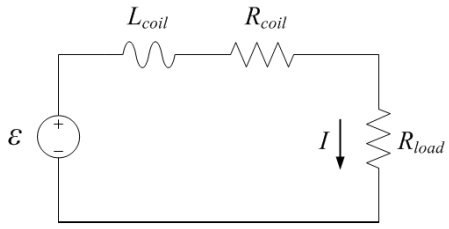

Figure 2.6. Load resistor circuit.

To find the circuit equation, one can apply Kirchhoff's voltage law by summing voltage rises clockwise around the circuit. This gives

$$\varepsilon - L_{coil}\,\dot{I} - R_{coil}\,I - R_{load}\,I = 0\,. \tag{2.35}$$

Invoking the coupling relation between the induced voltage and the radial velocity of the magnet,

$$\varepsilon = \alpha(r)\,\dot{r}\,, \tag{2.36}$$

the circuit equation becomes

$$L_{coil}\,\dot{I} + \left(R_{coil} + R_{load}\right)I = \alpha(r)\,\dot{r}\,. \tag{2.37}$$

Because the induced voltage depends upon the coupling factor and the radial velocity of the magnet, the current through the coil will depend upon the position and velocity of the magnet. The voltage across the load resistor (V_{load}) is

$$V_{load} = I\,R_{load}\,. \tag{2.38}$$

The potential useful power produced by the harvester is the power dissipated across the load resistor. This power (P_{load}) is

$$P_{load} = I^2 R_{load} = \frac{V_{load}^{\ 2}}{R_{load}}. \tag{2.39}$$

The total energy consumed by the load resistor (E_{load}) is

$$E_{load} = \int_{t=0}^{T} P_{load}\, dt, \tag{2.40}$$

where T is the run time of a numerical simulation or the run time of the experiment. The average power ($\overline{P}_{load}$) is this energy divided by the run time, or

$$\overline{P}_{load} = \frac{E_{load}}{T} = \frac{1}{T}\int_{t=0}^{T} P_{load}\, dt. \tag{2.41}$$

2.3.2 Energy Storage Circuit

Because the load resistor circuit only dissipates the generated energy, an energy storage circuit is needed. Sophisticated circuits have been developed to efficiently store electrical power and regulate the voltage to a load circuit [13, 14]. Here a basic energy storage circuit was implemented to simplify analysis and to demonstrate the harvester's ability to produce and store useful energy. Figure 2.7 shows the schematic of this circuit. The coil is again treated as an input voltage in series with an inductor and a resistor. The terminals of the coil are connected to a full wave rectifier, and the outputs of the rectifier are connected to a capacitor (C). The rectifier is a bridge circuit consisting of four diodes. An alternating current (I) enters the full wave rectifier and is converted into a direct current (I_C). The direct current from the rectifier maintains a consistent voltage polarity across the capacitor. This prevents the alternating current from the coil from damaging the capacitor. The diode bridge also prevents the capacitor from

discharging through the coil when energy is not being produced. There is a minimum voltage required to bias the diodes in the bridge. This results in some loss of output voltage from the rectifier and consequently some loss of energy. The stored energy on the capacitor can be used to power the SHM equipment when the turbine is not turning and the harvester is not producing energy. Although not used here, a rechargeable battery is often placed in parallel with this capacitor. In this case the battery stores the electrical power, and the capacitor serves to smooth the ripples of the output voltage from the rectifier.

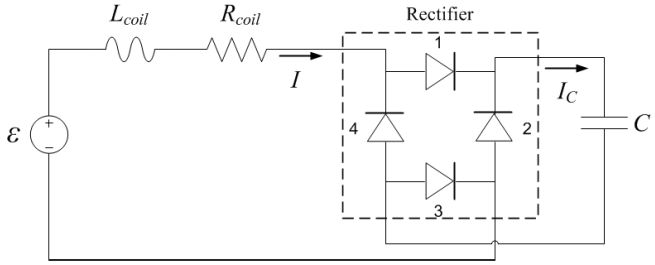

Figure 2.7. Basic energy storing circuit.

For the basic energy storage circuit in Figure 2.7, the amount of charge stored on the capacitor (q) is

$$q(t) = q(0) + \int_{t'=0}^{t} I_C \, dt' , \tag{2.42}$$

where $q(0)$ is the initial amount of charge on the capacitor and t' is a dummy variable. The energy stored on the capacitor (E_C) is

$$E_C = \frac{1}{2}\frac{q^2}{C} = \frac{1}{2} C V_C{}^2 , \tag{2.43}$$

where V_C is the voltage across the capacitor. This voltage is related to the charge as

$$V_C = \frac{q}{C} , \tag{2.44}$$

Let V_{bridge} be the voltage drop across the diode bridge (i.e. the voltage necessary to bias two of the diodes). Using Kirchhoff's voltage law, one can find the equations for the basic energy storage circuit in terms of the charge q. Because of the presence of the diode bridge, the circuit equations are determined by three possible scenarios. If the input voltage (ε) is greater than the sum of the voltage on the capacitor (V_C) and the bias voltage across the bridge (V_{bridge}), then current will flow through diodes 1 and 3 but not through diodes 2 and 4. If the input voltage is less than the negative of this voltage sum, then current will flow through diodes 2 and 4 and not diodes 1 or 3. If neither of these conditions is met, then current does not pass through any of the diodes, the capacitor, or the coil. Table 2.1 lists the circuit equations for these three possible scenarios.

Table 2.1. Circuit equations for the simple energy storage circuit.

Scenario	Circuit Equations
$\varepsilon > V_C + V_{bridge}$	$L_{coil}\frac{d^2q}{dt^2} + R_{coil}\frac{dq}{dt} + \frac{1}{C}q = \varepsilon - V_{bridge}$ $\frac{dq}{dt} = I_C = I$
$\varepsilon < -\left(V_C + V_{bridge}\right)$	$L_{coil}\frac{d^2q}{dt^2} + R_{coil}\frac{dq}{dt} + \frac{1}{C}q = -\varepsilon - V_{bridge}$ $\frac{dq}{dt} = I_C = -I$
$\lvert\varepsilon\rvert < V_C + V_{bridge}$	$\frac{dq}{dt} = I_C = I = 0$

2.4 Numerical Simulation

The equations governing the model appear as basic ordinary differential equations. However, the end conditions and the Coulomb friction force prevent a typical ordinary differential equation solver (such as MATLAB's ode45) from solving these equations. These complications require allowing the model to predict the state of the system, checking to see if the magnet is still inside the tube and if the forces on the magnet can overcome static friction, and then correcting the magnet's position and radial velocity if these conditions are not meet. Therefore a numerical solver was created using Euler's method for solving differential equations and a prediction-correction scheme. The MATLAB code of the numerical solver is presented in Appendix A.

Figure 2.8 shows a flowchart of the algorithm behind the numerical solver. The subscript i indicates the variable is evaluated at a discrete time t_i. The algorithm starts with the variables from the previous time step and the current input rotation speed. Next the algorithm uses this information to compute values for the coupling factor (α), the normal force (N), the kinetic friction force (F_f), and the applied force (F_p) on the magnet. Then the time is advanced by a small time step (Δt), and the previously calculated parameters are used to predict new values for the angle of the harvester (θ), the radial position of the magnet (r), and the radial velocity of the magnet ($\dot{r}$) at the new time value (t_{i+1}). Next the radial position of the magnet is compared to the minimum (r_1) and the maximum (r_2) allowable values. If the magnet has traveled outside these physical tube limits, the magnet is repositioned inside the tube and the radial velocity is set to zero. Next the static friction condition is checked. The magnet is held in place if the magnet was at rest at the previous time value and the applied force at the current time value is not

enough to overcome static friction. With the mechanics computed, the circuit equation calculates a value for the current in the coil based on the magnet's radial velocity and the value of the coupling factor. The circuit equation in Figure 2.8 governs the load resistor circuit. This equation can be replaced by the equations for the energy storage circuit when that circuit is in use. This sequence of procedures is repeated until the time reaches a predefined limit (T).

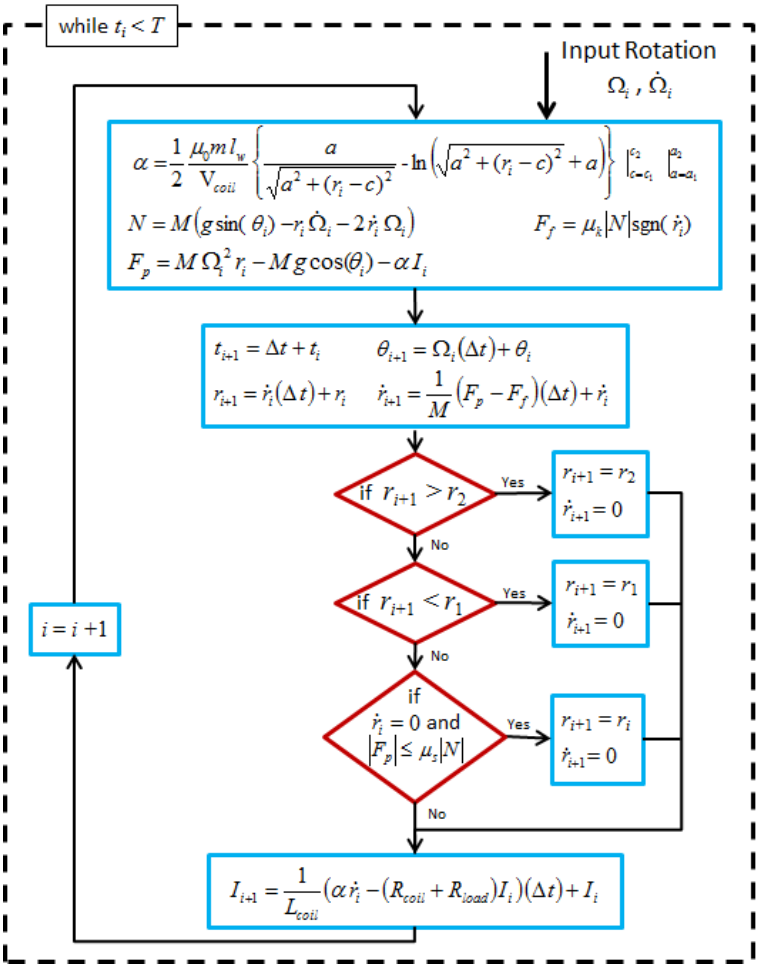

Figure 2.8. Algorithm for solving the harvester model.

To verify the code was working properly, the MATLAB code was used to simulate the rotation of an example harvester with a load resistor circuit. Figure 2.9 shows the path of the magnet inside the harvester for one rotation at 10 RPM. In the figure the harvester is rotating clockwise and the direction of gravity is downward. A black dot represents the starting location of the magnet, and the dark blue curve is the path of the magnet as it slides along the rotating tube. The tube limits are shown as concentric red rings while light blue rings indicate the radial positions of the bottom (c_1) and top (c_2) of the coil. The coil is centered in the middle of the tube and has a height of 30 mm. The figure shows that the magnet passes through the coil twice per rotation. Figure 2.10a shows the load voltage versus time for this simulated rotation. The two passes of the magnet through the coil induce two sets of voltage spikes. Figure 2.10b examines the second set of voltage spikes, and Figure 2.11 shows the same load voltage versus the radial position of the magnet. Here the magnet starts at r_1 and moves toward r_2. The voltage is nearly zero when the magnet is far away from the coil. As the magnet approaches the coil, the voltage increases, reaches a maximum when the magnet is at the entrance of the coil, and decreases as the magnet enters the coil. The voltage reaches zero when the magnet is in the middle of the coil. As the magnet travels away from the middle of the coil, the voltage continues to decrease, reaches a minimum when the magnet is at the exit of the coil, and increases toward zero as the magnet travels away from the coil.

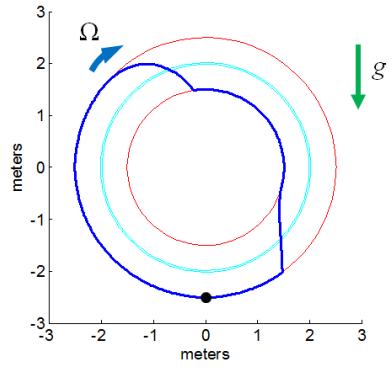

Figure 2.9. Trajectory of the magnet inside an example harvester.

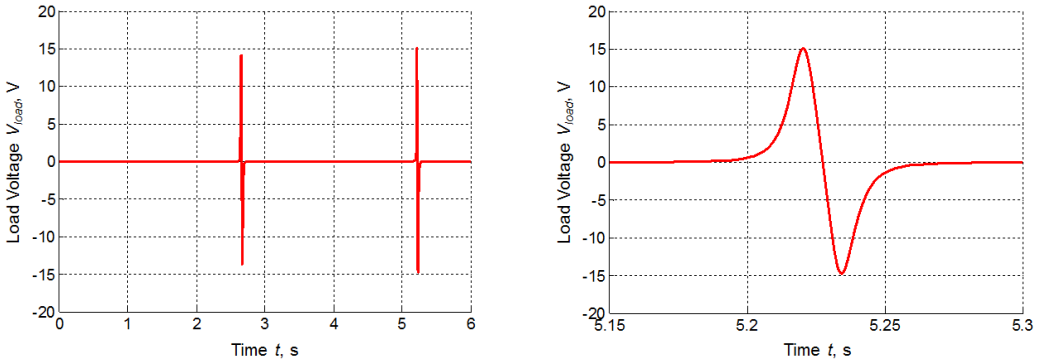

(a) (b)

Figure 2.10. (a) Numerical simulation of the voltage produced across a load resistor for an example harvester. (b) Plot showing only the second set of voltage spikes.

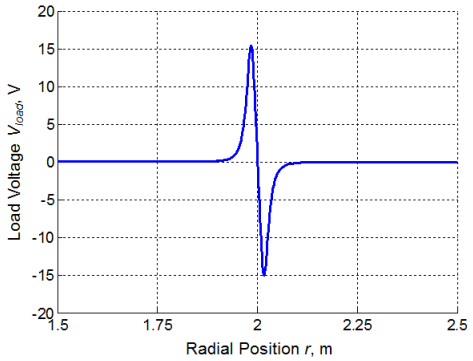

Figure 2.11. Load voltage versus the radial position of the magnet for Figure 2.10b.

2.5 Conclusion

This chapter presented a derivation of the energy harvester model. Newton's second law of motion led to an equation of motion for the magnet. A Coulomb friction force on the magnet was included in the model, and the end conditions were established to prevent the magnet from travelling outside of the tube. Next an electromechanical coupling factor was derived relating the motion of the magnet to the current in the electrical circuit. This nonlinear coupling factor was found through approximating the magnetic flux density of the magnet as originating from a magnetic dipole. The equations governing a load resistor circuit and a simple energy storage circuit were developed. Finally this chapter presented the algorithm used to solve the equations of the model. This algorithm used a prediction-correction method to predict the state of the system at a point in time, and then correct the system if the magnet travelled outside the tube or if the static friction condition was not met.

Chapter 3 Experimental Validation

Chapter 2 outlined the derivation of the energy harvester model. This chapter will focus on three experiments performed to validate this model. The first was a free fall test examining the electromechanical coupling factor between the circuit and the motion of the magnet. The second experiment examined the power output to a load resistor from a prototype harvester placed on a rotating wheel. The third experiment demonstrated the energy harvester's ability to charge a capacitor.

3.1 Free Fall Test

Before examining the full model of the energy harvester, it is necessary to validate the expression for the electromechanical coupling factor. A simple way to do this is to drop a magnet through a coil. The energy harvester model can be reduced to the case of a free falling magnet by setting the rotation rate and tube angle to zero. In this case Equation 2.5 becomes

$$M\ddot{r} + \alpha(r)I = -Mg\,, \tag{3.1}$$

where r is the radial position of the magnet, I is the current through the coil, M is the mass of the magnet, α is the electromechanical coupling factor, and g is the acceleration due to gravity. The circuit equations remain unaltered. This test will use the load resistor circuit, which is governed by Equation 2.37, namely

$$L_{coil}\,\dot{I} + \left(R_{coil} + R_{load}\right)I = \alpha(r)\,\dot{r}\,, \tag{3.2}$$

where L_{coil} is the coil inductance, R_{coil} is the coil resistance, and R_{load} is the load resistance. This free fall case produces a simpler motion of the magnet that is uncomplicated by the rotation of the harvester or friction from the tube wall. Ignoring these effects allows one to study the electromechanical coupling more directly.

3.1.1 Experimental Setup

Figure 3.1 shows the free fall test setup. The test setup consisted of a coil resting on a PVC pipe assembly. A neodymium magnet was released from an initial distance of 6.25 in above the table. The magnet fell vertically through the pipe and through the coil. If the magnet contacted the pipe wall, the test was rerun. The terminals of the coil were connected to varying load resistors, and the measured voltage across each load resistor was compared to the voltage predicted by the model. The energy dissipated through the load resistor was computed from the measured voltage using Equation 2.40. Five trials were performed for each load resistor, and the total energy dissipated for each resistance was averaged over all five runs. Table 3.1 lists the parameters for the free fall test. In this test the bottom of the tube was taken to be $r = 0$ in.

Figure 3.1. Free fall test assembly and a neodymium magnet.
A quarter is shown for size comparison.

Table 3.1. Measured parameters for the free fall test.

Magnet	
Height	0.75 in (19.1 mm)
Diameter	0.5 in (12.7 mm)
Mass (M)	18 grams
Initial distance above table	6.25 in (159 mm)
Coil	
Inner radius (a_1)	0.509 in (12.9 mm)
Outer radius (a_2)	1.02 in (28.1 mm)
Coil height (h)	1.17 in (29.7 mm)
Wire diameter (D_w)	0.0080 in (0.203 mm)
Coil resistance (R_{coil})	426 Ω
Coil inductance (L_{coil})	0.998 H
Distance from coil bottom to tube bottom (c_1)	2.50 in (63.5 mm)
Tube	
Total length (l)	6.00 in (152 mm)
Data Acquisition	
Sampling rate	1000 Hz

The only parameter in the model that cannot be easily measured was the magnetic dipole moment (m). The magnetic dipole moment of a permanent magnet can be estimated through the equation

$$m = \frac{B_r \mathrm{V}_m}{\mu_0}, \tag{3.3}$$

where B_r is the residual magnetic flux density of the permanent magnet, V_m is the volume of the magnet, and μ_0 is the permeability of free space [54]. The residual flux density for a neodymium magnet is around 1.15 T [56]. For the size of magnet from the free fall test, the magnetic dipole moment was estimated to be 2.21 A-m^2. However the magnetic dipole moment may differ from this calculated value due to variations in the residual magnetic flux density from manufacturer's specifications.

3.1.2 Results

Appendix B shows plots of the voltage across the load resistors tested. Figure 3.2a plots the voltage across a 555 Ω load resistor versus predictions from the model with a magnetic dipole moment of 2.21 A-m^2 and 2.1 A-m^2. Figure 3.2b shows the energy dissipated across varying load resistances compared to model predictions using these two dipole moment values. A magnetic dipole moment of 2.21 A-m^2 was estimated in Section 3.1.1. However the true magnet dipole moment differs from this due to variations in the strength of the magnet from the manufacturer's specifications. The value of 2.1 A-m^2 was determined by varying the value of *m* in the model until the predicted energy versus load resistance curve produced a close match to the data. The average error between the data and model with the calculated magnetic dipole moment of 2.21 A-m^2 was about 8%. The average error using a magnetic dipole moment of 2.1 A-m^2 was about 2%. Unless otherwise indicated, the magnetic dipole moment will be taken to be 2.1 A-m^2.

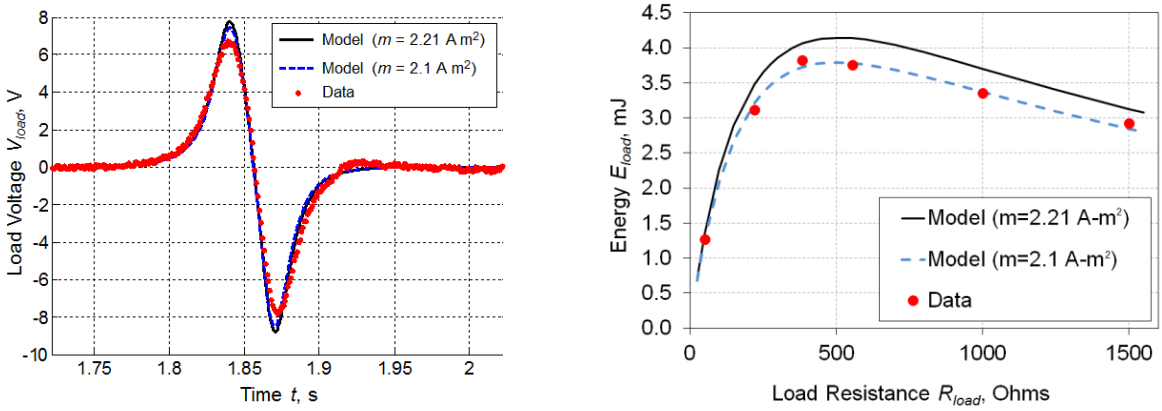

(a) (b)

Figure 3.2. (a) Voltage across a 555 Ω load resistor versus time for the free fall test. (b) Energy dissipated across varying load resistances.

These results demonstrated that the expression for the coupling factor (α) was sufficiently accurate for describing the nonlinear interaction between the magnet and the coil. From the model with the magnetic dipole moment of 2.1 A-m^2, the maximum energy dissipated across a load resistor would be 3.79 mJ at a load resistance of 500 Ω. At a load resistance equal to the resistance of the coil (426 Ω), the energy dissipated would be 3.77 mJ. The difference in energies from this value to the maximum dissipated energy is less than 1%. This is justification for using a load resistance equal to the coil resistance to estimate the maximum power output from the harvester in later analysis in Chapter 4.

3.2 Rotating Test

With the electromechanical coupling expression validated, the full model of the system could be tested. This section examines testing a prototype energy harvester inside a rotating test apparatus. The test setup created a rotating environment for the prototype harvester to study the power output to a load resistor as a function of rotation speed.

3.2.1 Experimental Setup

Figure 3.3 shows the rotating test setup developed to examine the full system model. The rotating apparatus incorporates components from an electric bicycle conversion kit. A prototype harvester was built consisting of a clear PVC pipe with a magnet on the inside and a coil mounted on the outside. The same coil and magnet were used in this test as in the free fall test.

The prototype harvester was positioned radially on the bicycle wheel. An electric motor spun the wheel, and a laser tachometer measured the wheel's rotation speed. A counterweight was used to balance the wheel, and a reflective patch for the tachometer was attached to a counterweight. The leads from the coil were connected to a 176 Ω load resistor (located behind the top battery in Figure 3.3). The voltage across this resistor was measured using a National Instruments WLS 9206 wireless data acquisition (DAQ) system. The wireless DAQ transmitted this voltage information to a laptop with a wireless card. The load voltage was recorded by a LabVIEW program while the wheel spun for 60 seconds at a desired speed. The load voltage was converted into an average load power using Equation 2.41. Table 3.2 shows the parameters for the rotating test.

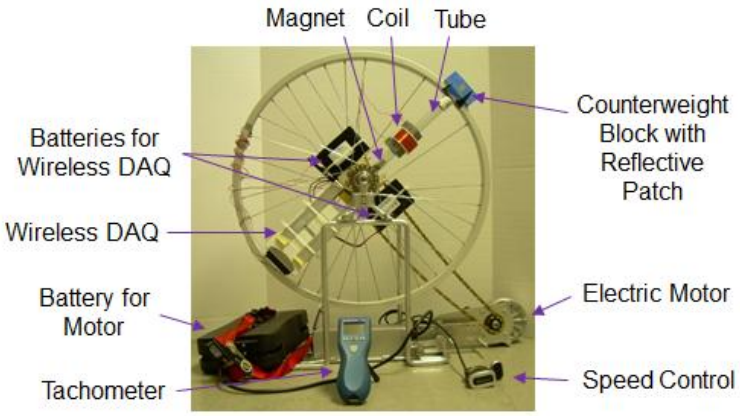

Figure 3.3. Rotating test apparatus and prototype harvester.

Table 3.2. Measured parameters for the rotating test.

Magnet	
Height	0.75 in (19.1 mm)
Diameter	0.5 in (12.7 mm)
Mass (M)	18 grams
Coil	
Inner radius (a_1)	0.509 in (12.9 mm)
Outer radius (a_2)	1.02 in (28.1 mm)
Coil height (h)	1.17 in (29.7 mm)
Wire diameter (D_w)	0.0080 in (0.203 mm)
Coil resistance (R_{coil})	426 Ω
Coil inductance (L_{coil})	0.998 H
Distance from coil bottom to center of rotation (c_1)	4.63 in (118 mm)
Tube	
Radial position of the bottom of the tube (r_1)	1.88 in (47.6 mm)
Radial position of the top of the tube (r_2)	9.26 in (235 mm)
Tube length (l)	7.38 in (187 mm)
Electrical Circuit	
Load resistance (R_{load})	176 Ω
Data Acquisition	
Sampling rate	5000 Hz

3.2.2 Results

Appendix C shows load voltage versus time plots for the prototype harvester at various rotation speeds. Figure 3.4 shows the average power dissipated across the load resistor versus rotation speed from the model and from the data. The plot also compares predictions from the model without friction and the model with friction. Starting with the wheel at rest, all three curves show that increasing the rotation rate increased the average dissipated power. The load power reached a maximum at a peak speed (designated as Ω_{peak}). Above the peak speed, there was a sharp decrease in the average load power. Around this speed, the centrifugal effect on the magnet began to overcome the effort of gravity to pull the magnet downward. Thus the magnet

did not fall completely to the bottom of the tube and consequently it did not build up as much speed. From the data and from the model with friction, gravity cannot overcome the static friction and the centrifugal effects on the magnet while the wheel turned above 50 RPM. In this case, the magnet remained at the outermost point of the tube (r_2).

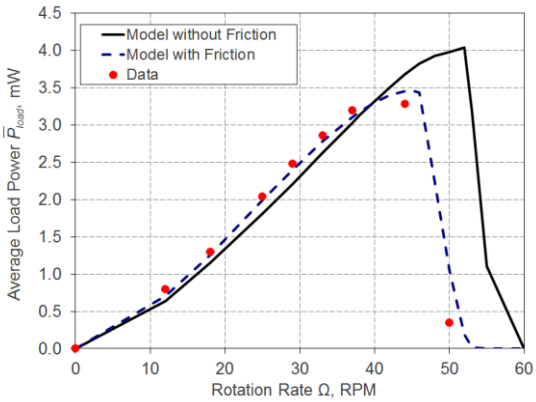

Figure 3.4. Average power across the load resistor versus rotation rate of the wheel.

The model without friction underestimated the power output from the prototype by about 10% on average for rotation speeds under 45 RPM. The frictionless model also predicted the harvester generating more power as the rotation speed increased from 45 RPM to 50 RPM while the data showed a sharp decline. The maximum power from the data was 3.3 mW at 44 RPM, while the frictionless model showed a maximum power output of 4.0 mW at 52 RPM. Due to the sharp decrease in output power, it is critical to correctly predict the location of the peak speed.

The discrepancy between the model and the data was corrected by including Coulomb friction to the model. The error between the data and the model with friction was about 3% excluding the data point at 50 RPM. Including friction also allowed the model to predict the

location of the peak in the data curve. The maximum average load power from the model with friction was 3.5 mW at 45 RPM. The static coefficient of friction was estimated by tilting the tube until the magnet began to slide and then measuring the inclination angle of the tube. From this approach the static coefficient of friction (μ_s) was determined to be around 0.35. The friction acting on the moving magnet was assessed by adjusting the kinetic coefficient of friction (μ_k) until the model with friction and the data were in close agreement. The kinetic coefficient of friction was estimated to be about 0.25. Unless otherwise stated, the model of the harvester will always include Coulomb friction with the stated values for the friction coefficients.

3.3 Capacitor Charging Test

To demonstrate that the harvester could produce useful electrical power for a SHM system, the prototype harvester and rotating test setup were used to charge a 0.1 F capacitor. The simple energy harvesting circuit was used in place of the load resistor from the previous tests. Several capacitors were tested, and the data from these tests are listed in Appendix D. Figure 3.5 plots the voltage across the capacitor while the wheel rotated at 17 RPM for 15 minutes. A rotation speed of 17 RPM was selected as it would be a rotation speed one might expect to see in a large scale wind turbine. To reduce the amount of data to process, the sampling rate was reduced to 25 Hz. The voltage drop across the rectifier bridge (V_{bridge}) was measured to be 0.6 V. After 15 minutes of rotation, the harvester charged the capacitor to 3.11 V (equivalent to 0.483 J of energy). The model overestimated the energy produced, and showed the capacitor charging to 3.38 V (equivalent to 0.571 J of energy). The error between predicted and measured energies was about 18%. This error was likely due to the capacitor's small self-discharge rate which was

not accounted for in the model. Figure 3.6a shows the voltage data and model prediction during testing. The wheel was stopped after 15 minutes of rotation, and the capacitor voltage was monitored for an additional five minutes. Figure 3.6b shows the capacitor's self-discharge while the wheel remained stationary. The model assumes an ideal capacitor that retains its voltage when not being charged. However the actual capacitor displays voltage loss when the harvester is not producing energy. This self-discharge can be reduced by using a rechargeable battery instead of a capacitor. Regardless of the discrepancy, this test showed the harvester could produce and store electrical energy.

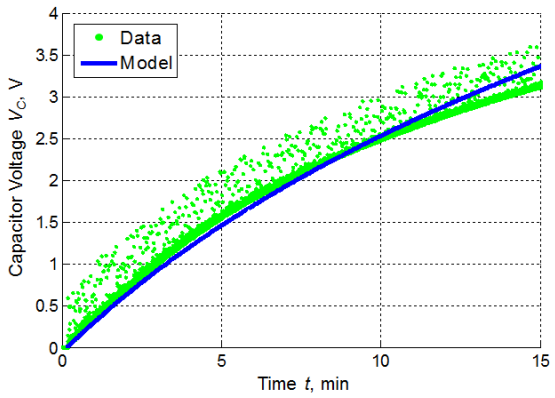

Figure 3.5. Voltage across the capacitor versus time.

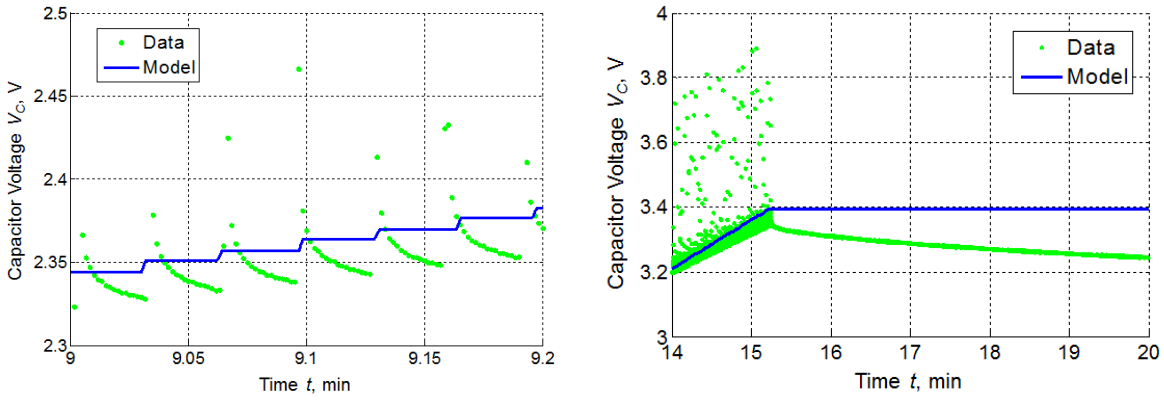

(a) (b)

Figure 3.6. (a) Voltage data and model prediction 9 minutes into the rotation test. (b) Data and model prediction while the wheel is at rest.

3.4 Conclusion

This chapter has presented results from three experiments designed to validate the energy harvester model. A free fall test validated the electromechanical coupling model. The magnetic dipole moment of the permanent magnet was determined to be 2.1 A-m^2 by examining the energy dissipated across six different load resistors. Next a rotating prototype tested the full model of the harvester with a load resistor. The model was able to predict the average power dissipated by the load resistor as a function of rotation speed. The model with friction predicted a maximum power output to 176 Ω load resistor of 3.5 mW at 45 RPM, while the data showed a maximum power output of 3.3 mW at 44 RPM. The results also showed the model needed a kinetic coefficient of friction of 0.25 and a static coefficient of friction of 0.35 in order to correctly predict the power versus rotation speed curve. Finally a capacitor charging test verified

the prototype harvester could store energy. Over a 15 minute test at 17 RPM, the prototype harvester was able to charge the 0.1 F capacitor to 3.11 V (0.483 J of energy). This was 18% less energy than predicted by the model, but this error was likely due to the capacitor's small self-discharge rate.

Chapter 4 Analysis of the Energy Harvester Model

With the model validated, one can proceed to examine energy harvesters for use inside a wind turbine blade. An effective energy harvester needs to be tailored to the characteristics of its host wind turbine. Knowledge of the wind turbine's range of rotation speeds, blade length, and hub size are vital for designing a functional harvester. This chapter will explore how various parameters affect the performance of the harvester and how to design the optimal harvester for a given wind turbine. First the harvester tube is examined. There are tradeoffs between the tube position, the tube length, and the maximum operating speed of the harvester. Next the coil design is studied. Altering the geometry and placement of a coil will affect the harvester's power output. Other properties of the harvester are studied, including the fill factor of the coil, the electrical resistivity of the wire, the magnetic dipole moment of the magnet, and the mass of the magnet. The friction coefficients will remain unaltered from the values determined in Section 3.2.2. Finally a sample harvester is presented that has the potential to power a structural health monitoring system over the full 0 RPM to 20 RPM target range.

4.1 Tube Design

The most critical component of the energy harvester is the tube design. The long length of the hollow wind turbine blades can accommodate long tube lengths; however this is not necessarily advantageous. If the magnet travels too far away from the center of rotation (i.e. the center of the hub) for a given rotation speed, then the centrifugal effects on the magnet will overwhelm the pull of gravity. The magnet will remain trapped at the outermost end of the tube,

and without the magnet's motion, the system cannot produce energy. Therefore it is important to begin by studying how the tube length and position affect the performance of the harvester.

4.1.1 Varying Tube Length and Position

Before continuing, a new performance metric for the harvester has to be established. While the power output of the harvester is important in the final design, it is not the best parameter to use in analyzing the role of tube length and position. The power output varies with rotation speed, tube length, and tube position. However, the power output also depends on the strength of the magnet, the design of the electrical circuit, the number of coils, the geometries and electrical properties of the coils, the positions of the coils along the tube, and the two friction coefficients. To remove this electrical dependency, the electromechanical coupling factor is set to zero in the model. Section 4.3 will show that a zero coupling factor also removes the influence of the magnet's mass on the performance of the harvester. Thus the motion of the magnet is reduced to being dependent only on the tube length, the tube position, the rotation speed of the harvester, and the friction coefficients. Without the coupling factor, there is no input voltage to the electrical circuit and thus no generated power. Consequently a new figure of merit that only depends on the motion of the magnet is needed.

From Chapter 2, the average power ($\overline{P}_{load}$) dissipated across the load resistor in the load resistor circuit is

$$\overline{P}_{load} = \frac{1}{T}\int_{t=0}^{T} \frac{V_{load}^{\ 2}}{R_{load}}\,dt\,, \tag{4.1}$$

where T is the run time of the simulation, V_{load} is the voltage across the load resistor, and R_{load} is the value of the load resistance. When the driving frequency is low, the coil inductance is often ignored to simplify analysis [26, 39, 48]. If the coil inductance is ignored, then the average load power can be written as

$$\overline{P}_{load} = \frac{1}{T}\int_{t=0}^{T} \alpha^2(r)\frac{R_{load}}{\left(R_{load}+R_{coil}\right)^2}\dot{r}^2 dt\,, \tag{4.2}$$

where α is the electromechanical coupling factor, r is the radial position of the magnet, and R_{coil} is the resistance of the coil. For a given coil and load resistor, it can be seen that increasing the average power is accomplished through increasing the average of the square of the magnet's radial velocity. Thus in place of electrical power, the goal in this section will be to maximize the root mean square (RMS) radial velocity of the magnet (v_{RMS}), defined as

$$v_{RMS} \equiv \sqrt{\frac{1}{T}\int_{t=0}^{T} \dot{r}^{\,2} dt}\,. \tag{4.3}$$

Increasing the RMS radial velocity of the magnet will result in an increase in power to a load resistor.

Next one can characterize how the RMS radial velocity changes with tube length and position. Figure 4.1a shows a schematic of the energy harvester without a coil inside a wind turbine blade. The figure shows the radial position of the bottom of the tube (r_1), the radial position of the top of the tube (r_2), and the tube length (l). These three parameters are related through

$$l = r_2 - r_1\,. \tag{4.4}$$

Figure 4.1b shows the RMS radial velocity of the magnet versus rotation speed of the harvester for varying tube lengths and positions. The velocity curves show the same characteristics as the power curves from Chapter 3. All of the RMS velocities increase for

increasing rotation speed of the turbine until a maximum value is reached. Further increasing rotation rate decreases the RMS velocity of the magnet. The rotation speed at which the maximum RMS velocity of the magnet occurs is designated as the velocity peak speed (Ω^{v}_{peak}). This is distinguished from the earlier peak speed (Ω_{peak}), which is defined as the speed at which the harvester produces the maximum average power to a load resistor. The values of these two rotation speeds will differ slightly. For a given tube length (curves with the same line color), moving the tube upward (by increasing r_1) decreases the velocity peak speed. This is because the maximum radial position of the magnet (r_2) has increased, and this causes the centrifugal effects near the outer end of the tube to become stronger at lower speeds. Otherwise, the RMS velocity curves for a given tube length nearly overlap for rotation speeds below their velocity peak speeds. For a given value of r_1 (curves of the same line style), increasing the tube length increases r_2 and consequently decreases the velocity peak speed. However, increasing the tube length increases RMS velocities below the velocity peak speed. These results show that the goal of designing the harvester tube is to make the tube as long as possible while keeping the velocity peak speed above the maximum rotation speed of the wind turbine.

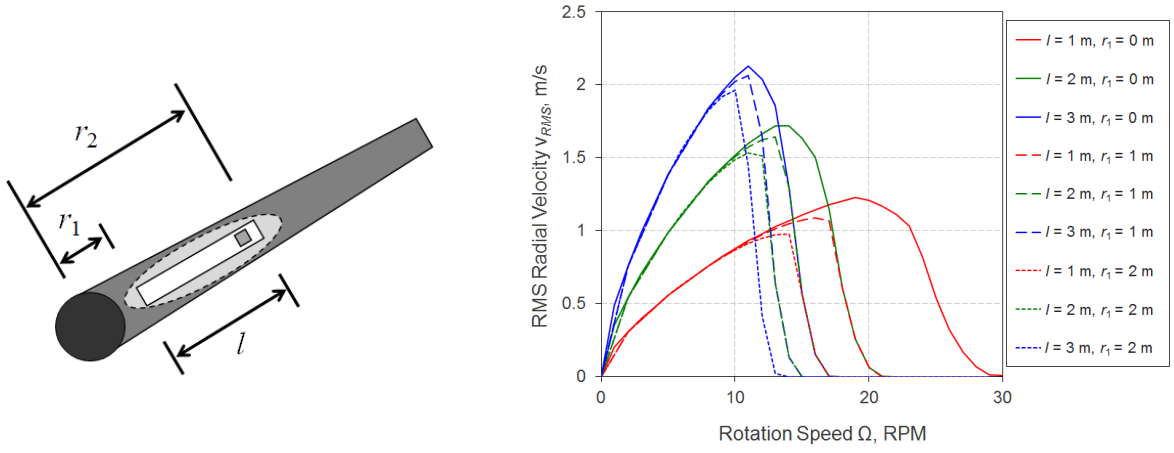

(a) (b)

Figure 4.1. (a) Diagram of the harvester without a coil. (b) Effect of varying tube geometry and placement on the RMS radial velocity of the magnet.

4.1.2 Determination of the Maximum Operating Speed

One can examine how the velocity peak speed changes with tube geometry by studying the velocity curves in Figure 4.1. Figure 4.2 plots the velocity peak speed versus the maximum radial position of the magnet (r_2) for various values of the minimum radial position (r_1). As expected the velocity peak speed decreases with increasing values of r_2. The figure also indicates the expected operating range of the wind turbine of 0 RPM to 20 RPM. Because of the sharp drop in the harvester's power output for rotation rates above the peak speed, the harvester tube should be designed with a velocity peak speed (which will be close to the peak speed) around or above 20 RPM. If the velocity peak speed is below 20 RPM, then the harvester may not produce enough power at the higher turbine speeds.

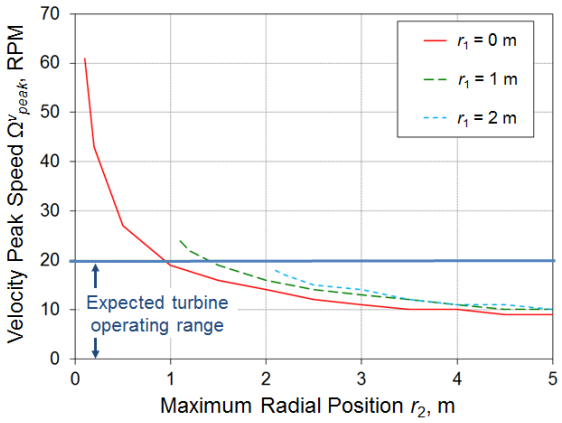

Figure 4.2. Velocity peak speed versus r_2 for varying r_1 values.

4.1.3 Tube Design for a Sample Harvester

From the set of velocity peak speed curves in Figure 4.2, one can design an appropriate energy harvester tube for use inside a given wind turbine blade. The hub of the wind turbine prevents the harvester from being positioned close to the center of rotation. An expected hub diameter is around 3 m [4]. Thus for this example harvester, the r_1 value was set to 1.5 m. The expected turbine operating range is 0 RPM to 20 RPM. To keep the velocity peak speed around 20 RPM, the tube length was set to 0.15 m. Figure 4.3 shows the average power to a load resistor and the RMS radial velocity of the magnet versus rotation rate for this sample harvester. The simulation uses the properties of the coil from Chapter 3 and places the coil at the center of the harvester tube. The magnet's mass and magnetic dipole moment remain unchanged from the tests in Chapter 3. The load resistance is set equal to the resistance of the coil. The RMS radial velocity curve does not include the electromagnetic drag force from the coil. Figure 4.3 shows that the peak speed and the velocity peak speed are about 19 RPM. The maximum average power to the matched load resistor is about 1.34 mW at 19 RPM. As presented, this sample

harvester can generate power over the entire desired range of turbine speeds. However power production can be improved by varying coil placement, coil size, the number of coils, and other properties of the system.

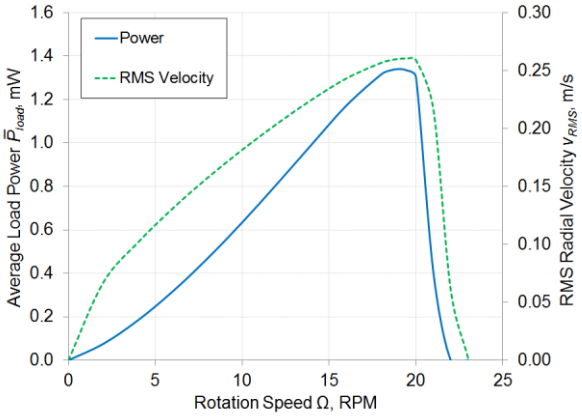

Figure 4.3. Average power and RMS radial velocity curves for the sample harvester with r_1 = 1.5 m and l = 0.15 m.

4.2 Coil Design

This section discusses the influence of varying the coil position and geometry on the power output of the harvester. Because the coils are in use, the output power to a load resistor can be considered instead of the RMS radial velocity of the magnet. First the effect of the coil position on the power output will be explored. Then the coil geometry will be varied to improve power production.

4.2.1 Varying Coil Position

For the sample harvester from Section 4.1.2, Figure 4.4 plots the average power to a matched load resistor versus the radial position of the center of the coil under a given rotation speed. The coil in the simulations is the same coil from Chapter 3 (inner radius of 12.9 mm, outer radius of 25.6 mm, and coil height of 30.2 mm). The coil and load resistances are 426 Ω. For low rotation speeds, the average power curve is nearly uniform except near the ends of the tube. Increasing the rotation speed increases the average power over the entire length of the tube, but the profile becomes less uniform. Near the peak speed, the average power curve is biased toward the upper end of the tube. The figure shows a significant drop in average power for all coil positions when the rotation speed is only 2 RPM greater than the peak speed.

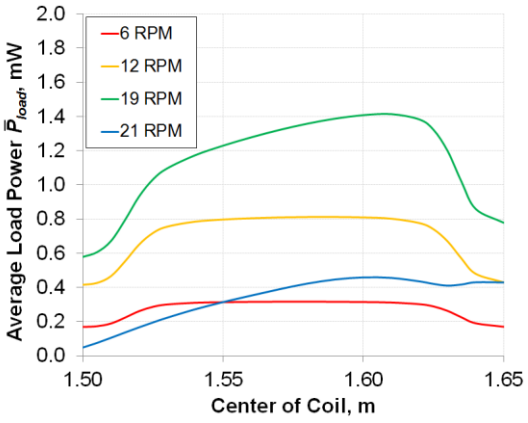

Figure 4.4. Average load power versus coil position for various rotation speeds.

Because of the short tube length in this harvester design, coils can be placed along the entire length of the sample harvester. For longer tubes, weight restrictions on the harvester and the cost of copper wire may prevent this approach. In this case only a few coils can be used.

Figure 4.4 indicates that the coils should be placed toward the outer end of the tube, but not too close to the end of the tube.

4.2.2 Varying Coil Size

Next the effect of the coil size on the power output is studied. Changing the size of the coil will alter some of the coil parameters. The fill factor (*FF*) of the coil is defined as ratio of the volume of the wire to the volume of the coil,

$$FF \equiv \frac{\mathrm{V}_w}{\mathrm{V}_{coil}} = \frac{\frac{\pi}{4} D_w{}^2 \, l_w}{\pi \, (a_2{}^2 - a_1{}^2) \, h}, \tag{4.5}$$

where V_w is the volume of the wire composing the coil, V_{coil} is the volume of the coil, D_w is the wire diameter, l_w is the total length of wire inside the coil, a_1 is the inner radius of the coil, a_2 is the outer radius of the coil, and h is the height of the coil. The fill factor is a measure of how efficiently the wire is packed into the coil volume. This expression was used to compute the fill factor of the coil from the experiments in Chapter 3 to be 0.56. The analysis in this section will leave the fill factor at 0.56 and the wire diameter at 0.008 in (32 gauge wire). The fill factor formula can be used to find the total length of the wire in the coil as

$$l_w = \frac{4 \, FF \, (a_2{}^2 - a_1{}^2) \, h}{D_w{}^2}. \tag{4.6}$$

From Zhu *et al.* [57], the number of turns of wire (n) can be found through the expression

$$n = \frac{l_w}{2\pi \, \bar{a}} = \frac{4 \, FF \, (a_2 - a_1) \, h}{\pi \, D_w{}^2}, \tag{4.7}$$

where $\bar{a}$ is the mean radius of the coil. The coil resistance is

$$R_{coil} = \rho \frac{l_w}{\left(\frac{\pi}{4} D_w^{\,2}\right)}, \tag{4.8}$$

where ρ is the electrical resistivity of the wire. This expression assumes the wire insulation is negligibly thin such that the total wire diameter (D_w) is the same as the diameter of the wire without insulation. The inductance of the coil (L_{coil}) is more difficult to determine. Based on formulas provided by Wheeler [58], the inductance can be estimated to be

$$L_{coil} \approx \frac{0.8x10^{-6}}{0.0254} \frac{\bar{a}^2 n^2}{6\bar{a} + 9h + 10(a_2 - a_1)}, \tag{4.9}$$

where the inductance is in henries and the length dimensions are in meters.

Using these formulas and the energy harvester model, one can study how the size of the coil affects the output power of the harvester. For simplicity, the inner radius of the coil (a_1) is kept at 12.9 mm. Changing the inner radius would correspond to a narrower tube and a smaller magnet. Thus changing the inner radius requires using a different magnet, and another complication would be introduced.

Figure 4.5a shows a schematic of a coil indicating the coil's inner radius (a_1), outer radius (a_2), and height (h). Figure 4.5b plots the average load power versus coil height for various outer coil radii. The model uses a load resistance equal to the coil resistance and places the coil in the center of the sample harvester from Section 4.1.3. Here the harvester spins at 12 RPM. For reference, the coil from the experiments in Chapter 3 had an outer radius (a_2) of 25.6 mm and a height (h) of 30.2 mm. Figure 4.5b shows that the maximum average power occurs for a coil with a height and an outer radius close to that of the original coil from Chapter 3. The figure also shows that increasing the outer radius for a given coil height increases the power output until a maximum is reached. Further increasing the outer radius will decrease the average power.

The outer radius increases when additional loops of wire are wound around the outside of the coil. The voltage induced in a loop of wire decreases as the radius of the loop increases because the wire is positioned further away from the magnet. Eventually the small additional voltage from adding more loops of wire does not compensate for the additional resistance added to the coil, and therefore the power output decreases.

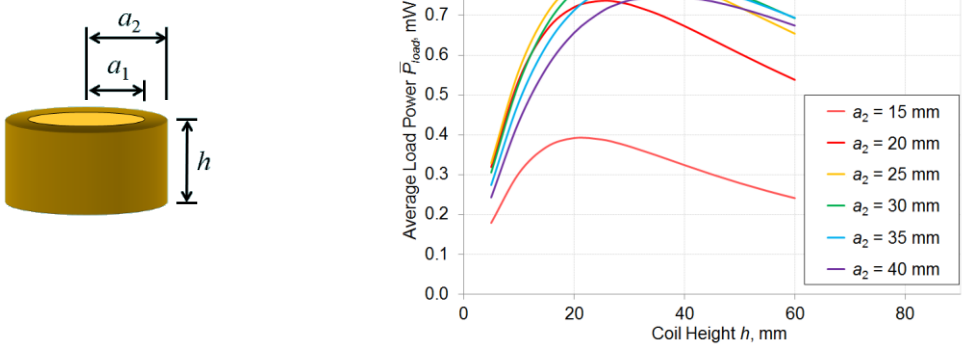

(a) (b)

Figure 4.5. (a) Diagram of a coil labeling a_1, a_2, and h. (b) Average power to a load resistor versus coil size.

If multiple coils are used, then the power output per coil is not necessarily the quantity of interest. For example, maintaining the original outer and inner radii but reducing the coil height from 30.2 mm to 15 mm decreases the power output from 0.820 mW to 0.701 mW. However the original coil can now be replaced by two coils of half the original height. These shorter coils would use the same amount of wire as the original coil, and therefore they would have the same total weight. The total output power from both of the shorter coils would be about 1.4 mW, which is a 70% increase from the single original coil. This leads to the conclusion that the power per coil height is a more useful figure of merit.

Figure 4.6 shows the power per coil height versus the coil height. Like the power curves in Figure 4.5b, the highest power per coil height occurs for an outer radius around 25 mm. However these plots show that decreasing the coil height increases the power per coil height for all values of the outer radius. This indicates that using multiple short coils would produce more power than using a few longer coils. From these results, new coils for the harvester were selected with an inner radius of 12.9 mm, an outer radius of 23 mm, and a height of 5 mm. Coils of smaller heights could be used, however this requires using more coils and using more complex electrical circuitry. With a tube length of 0.15 m, the harvester can fit thirty of the 5 mm coils.

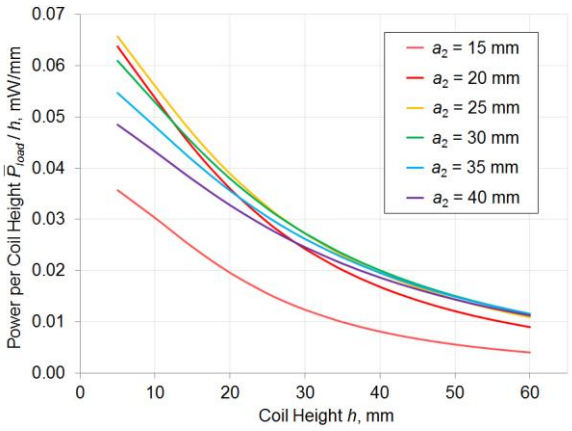

Figure 4.6. Power per coil height versus coil size.

There is an intuitive explanation why decreasing the coil height increases the power per coil height. Figure 4.7 shows a magnet moving with a velocity $\dot{r}$ between two rings from a coil. The magnet is centered between the two rings. The moving magnet induces a positive voltage in the ring in front of it and a negative voltage of the same magnitude in the ring behind it. If these rings are part of the same coil, then the total voltage of the coil would be the sum of the voltages from all of its rings. The voltages from the two rings in Figure 4.7 cancel each other in the

summation. Thus the total voltage and consequently the total power from the coil decrease while the magnet is inside the coil (this is seen in Figure 2.10 and Figure 3.2a). The voltage and power from the coil are zero when the magnet is in the center of the coil.

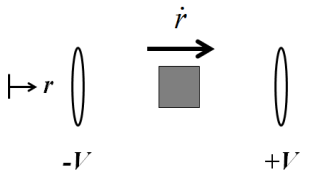

Figure 4.7. Magnet moving between two rings.

However, if the rings from Figure 4.7 are not connected together, then their voltages would not be added. In this case the total power output from the rings is simply the sum of the power outputs from each ring, which would be nonzero for any position of the magnet. Consequently a set of independent rings would have a higher total power output than if the rings were connected together in the same coil. Not all of the rings have to be independent. A set of connected concentric rings would not experience this total voltage reduction because this effect only occurs for rings at different distances from the magnet (different *z*-coordinates from Figure 2.4). Several of these flat coils would have a higher total power output than a single coil with all of its windings connected together despite the set of flat coils having the same total height as the single coil. Therefore the flat coil design has a higher power per coil height. Decreasing the height of a coil causes the coil to approach this optimal flat coil geometry. Thus the power per coil height increases with decreasing coil height.

4.3 Varying Other Parameters

Some parameters such as the coil's fill factor, the resistivity of the wire, the magnetic dipole moment of the permanent magnet, and the mass of the magnet are independent of the size and position of the coil or the tube. To see how these properties affect the harvester's power output, the average power to a load resistor is reexamined, namely

$$\overline{P}_{load} = \frac{1}{T}\int_{t=0}^{T} \alpha^2(r)\frac{R_{load}}{\left(R_{load}+R_{coil}\right)^2}\dot{r}^2 dt\,. \tag{4.10}$$

Let the load resistance equal the coil resistance. After substituting the earlier expressions for the electrical resistance and the length of wire, the average power becomes

$$\overline{P}_{load} = \frac{{\mu_0}^2 m^2 FF}{16\,\rho\,\mathrm{V}_{coil} T}\int_{t=0}^{T}\left\{\left[\frac{a}{\sqrt{a^2+(r-c)^2}} - \ln\left(\sqrt{a^2+(r-c)^2}+a\right)\right]\Big|_{c=c_1}^{c_2}\Big|_{a=a_1}^{a_2}\right\}^2 \dot{r}^{\,2} dt\,. \tag{4.11}$$

Note that the expression does not depend on the wire diameter (D_w). This indicates that the power output is independent of the wire diameter. The expression above hints that increasing the fill factor, increasing the magnetic dipole moment, or decreasing the resistivity should increase the power output. However, increased power output indicates an increase in the current flowing through the circuit. Increasing current results in a stronger electromagnetic drag force on the magnet, and this reduces the radial velocity of the magnet ($\dot{r}$). Thus there will be some complexity to the relationships between these parameters and the power output.

To illustrate this result, the free fall experiment is simulated with variations in magnetic dipole moments, fill factor, and resistivity. The load resistance is set to the resistance of the coil, which increases with increasing resistivity or increasing fill factor. For reference, the magnetic dipole moment was previously determined to be 2.1 A-m^2, the fill factor of the coil was estimated to be 0.56, and the electrical resistivity of the copper wire was taken to be

1.72 x 10^{-8} Ω-m [59]. Figure 4.8 shows the energy dissipated across a matched load resistor (426 Ω) versus the magnetic moment of the magnet. The other parameters are held constant. For small values of m, the energy curve follows an m^2 relationship as expected from Equation 4.11. However, the energy deviates from this relationship for increasing magnetic dipole moments. Figure 4.9 and Figure 4.10 show similar trends for varying the resistivity and fill factor, respectively. These figures also plot the value of the coil resistance.

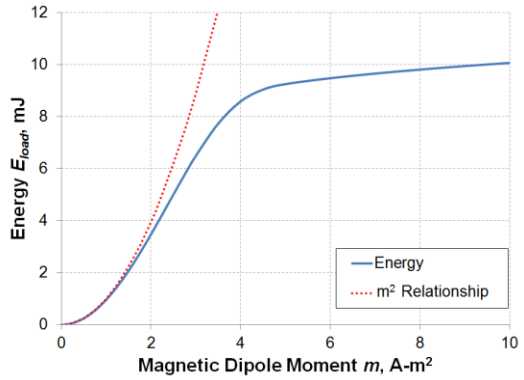

Figure 4.8. Simulation of the free fall experiment for varying magnetic dipole moments.

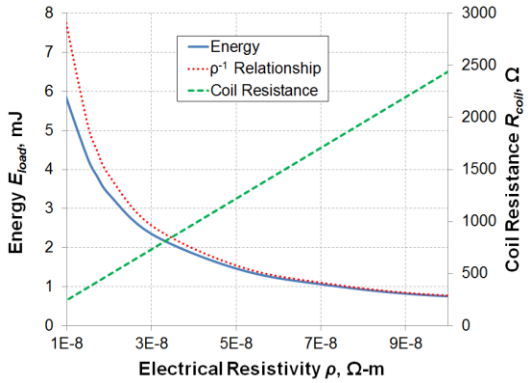

Figure 4.9. Simulation of the free fall experiment for varying electrical resistivities.

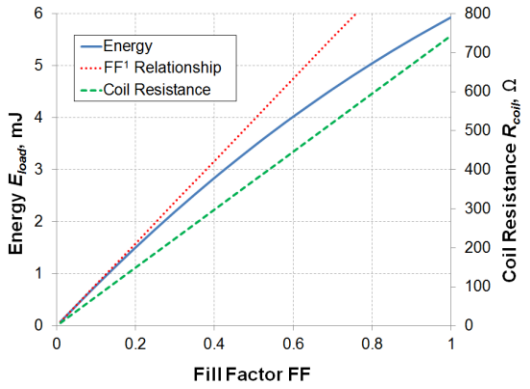

Figure 4.10. Simulation of the free fall experiment for varying fill factors.

It should be noted that the magnetic dipole moment can be increased by using a more highly magnetized material or by increasing the size of the magnet. A neodymium magnet, one of the most highly magnetized materials commercially available, was used throughout the experiments and in the model. Thus the most likely manner for increasing the magnetic dipole moment is to increase the size of the magnet. However increasing the size of the magnet will change other parameters, such as the magnet's mass and the inner radius of the coil. Likewise decreasing the electrical resistivity of the wire significantly would be difficult. The wire composing the coil is made from copper. Copper has the lowest resistivity of any metal at room temperature except for silver, which has a resistivity of 1.63×10^{-8} Ω-m [60]. To increase the fill factor, one must carefully wind the coil to minimize the space between windings. However, this is a tedious and time-consuming process. The coils from the experiments in Chapter 3 were scrabble wound to save production time. For the final design presented below, the fill factor, magnetic dipole moment, and resistivity parameters are unchanged from their previous values.

To study how changing the mass of the magnet affects the power output of the harvester, one can examine the equation of motion derived in Chapter 2,

$$M\ddot{r} - M\Omega^2 r + F_f + \alpha(r)I = -M g\cos(\theta), \tag{4.12}$$

where M is the mass of the magnet. Using the normal force expression, the force of friction (F_f) on the magnet while it is in motion is

$$F_f = \mu_k M \left| g\sin(\theta) - r\dot{\Omega} - 2\dot{r}\Omega \right| \operatorname{sgn}(\dot{r}) . \tag{4.13}$$

All of the terms in the equation of motion and the friction force expression are directly proportional to the mass of the magnet except for the electromagnetic drag force. One can divide the equation of motion by the mass of the magnet. If the magnetic dipole moment is held constant, then one observes that increasing the mass of the magnet decreases the influence of the electromagnetic drag force on the motion of the magnet. For very large masses, this term nearly vanishes from the equation of motion. Figure 4.11 shows the energy dissipated across a 426 Ω load resistor from the free fall experiment under varying magnet masses. Increasing the mass of the magnet increases the energy produced from the coil. The energy approaches a limit of about 4.3 mJ for very large magnet masses. For the sample harvester in the next section, the magnet's mass was kept at its original 18 grams.

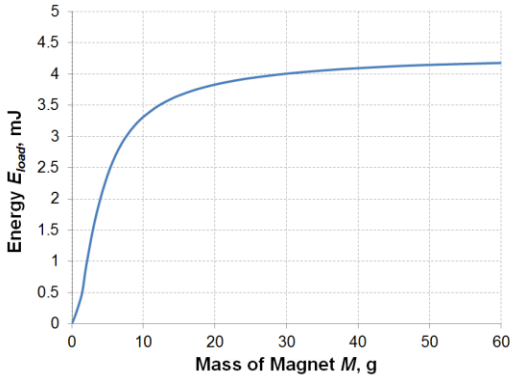

Figure 4.11. Simulation of the free fall experiment for varying magnet masses.

4.4 Final Design of the Sample Harvester

The sample harvester from Section 4.1.3 is combined with the short coils from Section 4.3. The harvester has a length of 0.15 m and has a bottom radial position (r_1) of 1.5 m. The short coils have an inner radius of 12.9 mm, an outer radius of 23 mm, and a height of 5 mm. A total of thirty coils were stacked over the entire length of the tube. The harvester was simulated for each coil with a matched load resistance (51.5 Ω), and the power outputs from all of the coils were added together. Figure 4.12 plots the total output power from the sample harvester and the magnet's RMS radial velocity versus rotation speed. The velocity curve assumes no coils are in place on the harvester. The harvester is able to produce power in the desired 0 RPM to 20 RPM range. The maximum power output is 14.1 mW at 19 RPM. This is over ten times the power output of the original sample harvester in Section 4.1.3.

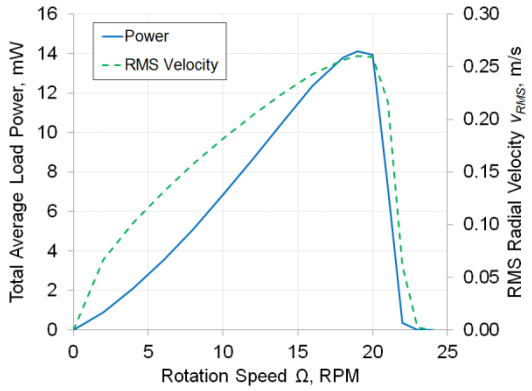

Figure 4.12. Total power output of the sample energy harvester and RMS radial velocity of the magnet.

Based on the density of copper of 8.9 g/cm^3 [59], the total mass of the harvester is about 1.6 kg. The mass of the SHM system is around 0.4 kg [11]. Thus the harvester adds a negligible amount of weight compared to the 40,000 kg to 110,000 kg mass of a typical rotor on a large scale wind turbine [4, 61]. In addition the harvester and SHM equipment will add imbalance the rotor. The degree of allowable imbalance of a rotating machine can be rated by a balance quality grade (G). This grade is selected by an engineer for a given rotating device based on guidelines from ISO 1940/1 [61, 62]. A machine which is more sensitive to imbalances will have a lower balance quality grade. This grade is used to find the allowable level of imbalance through the inequality

$$G \geq e\,\Omega, \tag{4.14}$$

where Ω is the rotation rate of the rotor in radians per second and e is the distance from the axis of rotation to the center of mass of the rotor and the additional equipment. The distance e is found through

$$e = \frac{M_{harv}\left(\frac{r_1 + r_2}{2}\right) + M_{SHM}\, r_{SHM}}{M_{rotor} + M_{harv} + M_{SHM}}, \tag{4.15}$$

where M_{rotor} is the mass of the rotor without the harvester and SHM equipment, M_{harv} is the mass of the harvester, M_{SHM} is the mass of the SHM system, and r_{SHM} is the radial position of the SHM system. For a large scale wind turbine, the balance quality grade (G) is selected to be 16 mm/s [61]. Taking the mass of the rotor to be 40,000 kg, the radial position of the SHM system to be 1.5 meters, and the rotation speed of the turbine to be 20 RPM, the product $e\,\Omega$ is approximately 0.16 mm/s, which is significantly lower than the maximum allowable value of 16 mm/s. The moving magnet would contribute an additional imbalance to the rotor which changes with the

magnet's radial position. However this imbalance is insignificant due to the magnet's 18 gram mass. Thus the harvester and the SHM equipment add negligible imbalance to the rotor.

The power curve in Figure 4.12 gives the sum of the power outputs from the coils to matched load resistors. However, an energy storage circuit would be needed if harvester is to power a structural health monitoring (SHM) system. Because of the use of multiple coils, this circuit would be more complex than the simple energy storage circuit from Chapter 2. Furthermore adding together the power outputs from simulations that use only one coil at a time ignores the mutual inductance between coils in the final design. Nonetheless this effect should not severely impact the harvester's performance. Often mutual inductance is considered negligible for energy harvesters employing multiple coils [26, 35].

To operate continuously, an acoustic emission SHM system would require between 100 mW and 500 mW [11, 12]. Due to the variability in wind speeds, the turbine will not spin at a constant speed. Therefore the strategy for powering the SHM system would be to use an energy storage circuit and employ a duty cycle system. While the duty cycle is in the off-phase, the harvester can charge its capacitors. When the capacitors are charged and the duty cycle switches into the on-phase, the capacitors can power the SHM equipment. The SHM equipment does not need to continuously check the structural integrity of the blade, and hence these systems can use very low duty cycles [63, 64]. An SHM system would only need to check for damage and broadcast gathered information to a receiver unit for a few minutes per day. This gives the harvester plenty of time to charge its capacitors. With the duty cycle system, the harvester should be capable of powering the SHM equipment.

4.5 Procedure for Designing a Harvester

This chapter has discussed how changing various parameters will affect the performance of the harvester. A designer does not need to perform all of this analysis when creating an energy harvester for a given wind turbine. To design a harvester, the following procedure can be used.

1. Acquire information about the wind turbine, such as the range of rotation speeds and the size of the hub.
2. Select a proper tube length and position. The velocity peak speed of the harvester should be at or above the desired maximum operating speed.
3. Place the coils where the system produces the highest power. If only a few coils can be used, coils similar to those from the experiments in Chapter 3 can be used. These coils produced the maximum power output per coil. If multiple coils can be stacked along the harvester, then smaller coils should be used to produce a higher total power output.
4. Design an electrical circuit to store the produced energy from multiple coils and regulate the voltage to the SHM equipment.

4.6 Conclusion

With the energy harvester model derived and validated, parameters in the model were varied to study how the energy harvester would perform inside a large scale wind turbine blade. First the effect of varying the tube length and position on the performance and maximum

operating speed were studied. The velocity peak speed decreased as the outer end of the tube moved further away from the center of rotation. A tube with a length of 0.15 m placed 1.5 m from the center of rotation was selected to generate power over the 0 RPM to 20 RPM target range of rotation speeds. Next the position of the coil was varied. The results showed that coils placed toward the outer end of the harvester will produce more power at higher speeds. Varying the coil size showed the original coil from the experiments in Chapter 3 was near the optimal coil geometry to produce the highest power output per coil. It was discovered that decreasing the coil height increased the power per height of coil. This indicated that using multiple short coils would produce more power than using a few longer coils. Next the energy dissipated to a load resistor in the free fall experiment was studied under variations in other parameters. Increasing the magnetic dipole moment of the magnet, increasing the mass of the magnet, increasing the fill factor of the coil, or decreasing the electrical resistivity of the wire increased the energy produced. Next an energy harvester was presented that used thirty, 5 mm tall coils to generate up to 14.1 mW at 19 RPM. While it cannot power the structural health monitoring system continuously, the harvester could power the SHM equipment if an energy storage circuit and a duty cycle system are employed. This chapter concluded with a procedure to design a harvester for a selected wind turbine.

Chapter 5 Conclusions

This thesis has presented the development and analysis of a linear inductive energy harvester for powering structural health monitoring (SHM) equipment inside a wind turbine blade. This final chapter will give a brief overview of the research presented in this thesis, address how this work contributes to field of electromagnetic energy harvesting and other applications, and present some possibilities for future research.

5.1 Brief Summary of Thesis

Chapter 1 provided the motivation for this research, an overview of energy harvesting, and a brief literature review of electromagnetic energy harvesters and energy harvesters inside rotating environments. Several researchers have examined energy harvesters which could generate power inside a wind turbine blade. However, none of these harvesters produced significant power outputs around the expected operating speeds of large scale wind turbines (20 RPM and below).

In Chapter 2 a mathematical model was derived to describe the energy harvester. Newton's second law of motion produced an equation dictating the movement of the magnet. A coupling factor was derived relating the radial velocity of the magnet to the induced voltage in the coil. This factor also related the current in the coil to the electromagnetic drag force on the permanent magnet. Next a load resistor circuit and a simple energy storage circuit were examined. The load resistor circuit was useful for studying and validating the energy harvester model, while the energy storage circuit was necessary for storing the generated electrical energy.

Kirchhoff's voltage law gave the governing equations for these circuits. A MATLAB code used the model equations to compute the current state of the system while accounting for the ends of the tube and the static friction on the magnet.

Chapter 3 focused on experimentally validating the model. First a free fall test was used to verify the coupling factor expression. The model with a magnetic dipole moment of 2.1 A-m^2 closely matched the results obtained from the free fall experiment. Next a rotating prototype harvester was used to test the model with the load resistor circuit. The prototype was used to measure the power dissipated across a load resistor as a function of rotation speed. Using a static coefficient of friction of 0.35 and a kinetic coefficient of friction of 0.25, the model was able to match the experimental data within an average error of 4%. The model predicted the harvester would produce a maximum power output of 3.5 mW at 45 RPM to a 176 Ω load resistor. The data showed a maximum power output of 3.3 mW at 44 RPM. The rotating harvester with the simple energy storage circuit was used to charge a 0.1 F capacitor. The system was able to charge the capacitor to 3.11 V (0.483 J of energy) after spinning at 17 RPM for 15 minutes. This was about 18% below the estimated energy production from the model (0.571 J), but this discrepancy was likely due to the self-discharge of the capacitor.

Chapter 4 explored the performance of the harvester while varying parameters in the model. Plots of the root-mean-square (RMS) radial velocity of the magnet versus tube length and position showed the impact of the tube geometry on the velocity peak speed (the rotation speed at which the harvester will produce the highest RMS radial velocity). In general increasing the radial position of the top of the tube decreased the velocity peak speed. This information was used to design a 0.15 m long sample harvester with a bottom radial position of 1.5 m that could operate over the desired range of rotation speeds up to 20 RPM. Next a plot of

the power output versus coil position revealed the maximum power output per coil occurs for coils toward the far end of the tube. Varying the coil geometry revealed that the maximum power output per coil occurs for a coil around the same size as the coil from the tests in Chapter 3 (an inner radius of 12.9 mm, an outer radius of 25.6 mm, and a height of 30.2 mm). When stacking multiple coils along the harvester, the power per coil height becomes a useful figure of merit. The power per coil height increases with decreasing coil height. This was used to design a shorter coil for the harvester (an inner radius of 12.9 mm, an outer radius of 23 mm, and a height of 5 mm). Next the model was used to study the influence of other system parameters on the energy generated from the free fall experiment. The energy output increased for increasing fill factor of the coil, increasing magnetic dipole moment of the magnet, increasing mass of the magnet, and decreasing electrical resistivity of the wire. Then a sample energy harvester using thirty of the 5 mm coils was presented. This harvester could produce up to 14.1 mW at a peak speed of 19 RPM. With the help of an energy storage circuit and a duty cycle system, this harvester should be capable of powering a structural health monitoring system. Finally Chapter 4 concluded by presenting a procedure for designing an energy harvester for given wind turbine.

5.2 Contributions

This research has produced an electromagnetic energy harvester which should be able to power a structural health monitoring system inside a wind turbine blade. The SHM system can alert technicians of damage to the blade before catastrophic failure occurs. These systems improve the reliability of the turbine while reducing maintenance and inspection costs. The use

of an energy harvester could potentially eliminate the need for chemical batteries or installing a slip-ring between the turbine nacelle and the hub. This energy harvester design can be tailored to large scale wind turbines or other low speed rotating devices of various sizes and operating speeds. Unlike the energy harvesters examined in Chapter 1, this harvester is capable of generating several milliwatts at rotation speeds less than 60 RPM.

The model of the energy harvester is useful in other applications. By setting the rotation rate to zero, the model can describe a non-rotating linear harvester titled to any angle. The model includes Coulomb friction from the tube wall and the kinematic constraints from the end of the tube. Often energy harvesters will ignore these effects. Including Coulomb friction and the end conditions allows the model to describe a more realistic motion of the magnet inside the harvester. The model can easily be amended to include a spring or to account for base excitation. The electromechanical coupling expression can be incorporated into models of other electromagnetic energy harvesters to more accurately describe the nonlinear interaction between the moving magnet and the current flowing through the coil.

5.3 Recommendations for Future Work

In Chapter 4 the energy harvester model was used to simulate the power output of a sample harvester inside a large scale wind turbine. The model predicted the harvester with a duty cycle system could power the SHM equipment. To ensure this prediction is accurate, it is necessary to place the harvester inside a wind turbine blade and attempt to power a SHM system. In addition, the final harvester design requires sophisticated electrical circuitry to combine the

power outputs from multiple coils. This circuitry was not explored in this research, but this work would be necessary to build a harvester with more than one coil.

There are opportunities for improvements to the energy harvester model. The algorithm behind the model used Euler's method to solve the governing differential equations. This method is more accurate when small time steps are used, however smaller time steps result in longer simulation times. A faster and more accurate algorithm could be developed based on Runge-Kutta methods. In addition the model does not account for the presence of multiple coils in the final design. A model that allows the user to implement multiple coils on the harvester would yield more accurate predictions for the total power output from the system.

There are possible methods for further improving the performance of the energy harvester. As the magnet slides along the tube, the magnet can reach high instantaneous velocities. However, much of this kinetic energy is lost when the magnet impacts the ends of the tube. Several options exist for capturing this wasted energy. Piezoelectric harvesters on the ends of the tube, such as those used by Manla *et al.* [44], could convert the impacts of the magnet into useful electrical energy. Another option is to include additional magnets at the ends of the tube. These magnets would push the slider magnet toward the center of the harvester and therefore create a spring-like restoring force on the magnet. This would cause the slider magnet to oscillate near the ends of the tube and therefore pass through some of the coils several additional times per rotation. The additional oscillations of the magnet could produce a higher average power output than the harvester without the end magnets. A comprehensive study of various energy harvester designs (such as rotational or pendulum-based harvesters) in low speed rotating environments may produce a harvester with a higher power output than the linear harvester used here.

Bibliography

[1] C. C. Ciang, J.-R. Lee and J.-H. Bang, "Structural health monitoring for a wind turbine system: a review of damage detection methods," *Measurement Science and Technology*, vol. 19, 2008.

[2] American Wind Energy Association, "Industry Statistics," 2011: http://www.awea.org/learnabout/industry_stats/index.cfm.

[3] GE Energy, "GE Energy 3.6 MW offshore series wind turbine," University of Delaware, 2005. http://www.ceoe.udel.edu/windpower/docs/ge_36_brochure_new.pdf.

[4] J. Jonkman, S. Butterfield, W. Musial and G. Scott, "Definition of a 5-MW reference wind turbine for offshore system development," National Renewable Energy Laboratory, Golden, Coloroado, 2009.

[5] C. W. Pitchford, *Impedance-based structural health monitoring of wind turbine blades*, 2007.

[6] T. Simmermacher, G. H. James III and J. E. Hurtado, "Structural health monitoring of wind turbine blades," Sandia National Laboratory, Albuquerque, NM, 1997.

[7] Gurit, "Comparative cost study of a 35 m wind turbine blade using infusion and prepreg materials technology," http://www.gurit.com/files/documents/6_Cost_Study_Infusion_vs_Prepreg.pdf.

[8] L. Fingersh, M. Hand and A. Laxson, "Wind turbine design cost and scaling model," National Renewable Energy Laboratory, Golden, Colorado, 2006.

[9] G. Park, C. R. Farrar, M. D. Todd, W. Hodgkiss and T. Rosing, "Energy harvesting for structural health monitoring sensor networks," Los Alamos National Laboratory, 2007.

[10] Transtech Power Transmissions, "Flexible pin," http://www.transtech.no/flexiblepin.

[11] Physical Acoustics Corporation, "1282 acoustic emission wireless node and system," 2009. http://www.mistrasgroup.com/products/company/publications/2$Acoustic_Emission/1282_Wireless.pdf.

[12] Physical Acoustics Corporation, "USB AE node," 2009. http://www.mistrasgroup.com/products/company/publications/2$Acoustic_Emission/USB_AE_Node.pdf.

[13] R. Amirtharajah and A. P. Chandrakasan, "Self-powered signal processing using vibration-based power generation," *IEEE Journal of Solid-state Circuits*, vol. 33, no. 5, pp. 687-695, 1998.

[14] D. J. Inman and P. S, *Energy Harvesting Technologies*, New York, NY: Springer, 2009.

[15] J. R. Farmer, *A comparison of power harvesting techniques and related energy storage issues*, 2007.

[16] S. P. Beeby, M. J. Tudor and N. M. White, "Energy harvesting vibration sources for microsystems applications," Measurement Science and Technology, vol. 17, pp. 175-195, 2006.

[17] L. Wang and F. G. Yuan, "Energy harvesting by magnetostrictive material (MsM) for powering wireless sensors in SHM," in Proceedings of SPIE 6529: 652941, 2007.

[18] E. O. Torres and G. A. Rincón-Mora, "Electrostatic energy harvester and li-ion charger circuit for micro-scale applications," in 49th IEEE International Midwest Symposium on Circuits and Systems, San Juan, Puerto Rico, 2006.

[19] C. Byrne, "A Brief History of Electromagnetism," University of Massachusetts Lowell, 15 January 2011. http://faculty.uml.edu/cbyrne/EMHIST.pdf.

[20] D. P. Arnold, "Review of microscale magnetic power generation," *IEEE Transactions on Magnetics*, vol. 43, no. 11, pp. 3940-3951, 2007.

[21] P. D. Mitcheson, T. C. Green, E. M. Yeatman and A. S. Holmes, "Architectures for vibration-driven micropower generators," *Journal of Microelectromechanical Systems*, vol. 13, no. 3, pp. 429-440, 2004.

[22] P. D. Mitcheson, *Analysis and optimisation of energy-harvesting micro-generator systems*, 2005.

[23] C. B. Williams and R. B. Yates, "Analysis of a micro-electric generator for microsystems," in Transducers 95 - Eurosensors IX, Stockholm, Sweden, 1995.

[24] C. B. Williams and R. B. Yates, "Analysis of a micro-electric generator for microsystems," *Sensors and Actuators A: Physical*, vol. 52, pp. 8-11, 1996.

[25] C. B. Williams, C. Shearwood, M. A. Harradine, P. H. Mellor, T. S. Birch and R. B. Yates, "Development of an electromagnetic micro-generator," IEEE Proc. - Circuit Devices Syst., vol. 148, no. 6, pp. 337-342, 2001.

[26] L. Zuo, B. Scully, J. Shestani and Y. Zhou, "Design and characterization of an electromagnetic energy harvester for vehicle suspensions," *Smart Materials and Structures*, vol. 19, 2010.

[27] J. Prudell, M. Stoddard, E. Amon, T. K. A. Brekken and A. von Jouanne, "A permanent-magnet tubular linear generator for ocean wave energy conversion," *IEEE Transactions on Industry Applications*, vol. 46, no. 6, pp. 2392-2400, 2010.

[28] O. Danielsson, *Design of a linear generator for wave energy plant*, 2003.

[29] H. Polinder, M. Damen and F. Gardner, "Linear PM generator system for wave energy conversion in the AWS," *IEEE Transactions on Energy Conversion*, vol. 19, no. 3, pp. 583-589, 2004.

[30] Seiko, "Seiko Kinetic," http://www.seikowatches.com/technology/kinetic/.

[31] E. M. Yeatman, "Energy harvesting from motion using rotating and gyroscopic proof masses," *Proc. IMechE, Part C: J. Mechanical Engineering Science*, vol. 222, no. 1, pp. 27-36, 2008.

[32] A. Z. Trimble, J. H. Lang, J. Pabon and A. Slocum, "A device for harvesting energy from rotational vibrations," *Journal of Mechanical Design*, vol. 132, 2010.

[33] D. Spreemann, B. Folker, D. Mintenbeck and Y. Manoli, "Novel non-resonant vibration transducer for energy harvesting," in PowerMEMS 2005, Tokyo, Japan, 2005.

[34] M. El-hami, P. Glynne-Jones, N. M. White, M. Hill, S. Beeby, E. James, A. D. Brown and J. N. Ross, "Design and fabrication of a new vibration-based electromechanical power generator," *Sensors and Actuators A: Physical*, vol. 92, pp. 335-342, 2001.

[35] B. Yang, C. Lee, W. Xiang, J. Xie, J. H. He, R. K. Kotlanka, S. P. Low and H. Feng, "Electromagnetic energy harvesting from vibrations of multiple frequencies," *Journal of Micromechanics and Microengineering*, vol. 19, 2009.

[36] V. R. Challa, M. G. Prasad and F. T. Fisher, "A coupled piezoelectric-electromagnetic energy harvesting technique for achieving increased power output through damping matching," *Smart Materials and Structures*, vol. 18, 2009.

[37] B. Yang, C. Lee, W. L. Kee and S. P. Lim, "Hybrid energy harvester based on piezoelectric and electromagnetic mechanisms," *J. Micro/Nanolith. MEMS MOEMS*, vol. 9, no. 2, 2010.

[38] C. Carlson, A. Schlichting, S. Ouellette, K. Farinholt and G. Park, "Energy harvesting to power sensing hardware onboard wind turbine blade," in IMAC XXVIII, Jacksonville, FL, 2010.

[39] S. D. Conrad, *Development of an inertial generator for embedded applications in rotating environments*, 2007.

[40] T. T. Toh, A. Bansal, G. Hong, P. D. Mitcheson, A. S. Holmes and E. M. Yeatman, "Energy harvesting from rotating structures," in PowerMEMS 2007, Freiburg, Germany, 2007.

[41] T. T. Toh, P. D. Mitcheson, A. S. Holmes and E. M. Yeatman, "A continuously rotating energy harvester with maximum power point tracking," *Journal of Micromechanics and Microengineering*, vol. 18, 2008.

[42] T. T. Toh, P. D. Mitcheson and E. M. Yeatman, "Continuously rotating energy harvester with improved power density," in PowerMEMS, Sendai, Japan, 2008.

[43] Y.-J. Wang, C.-D. Chen and C.-K. Sung, "Design of a frequency-adjusting device for harvesting energy from a rotating wheel," *Sensors and Actuators A: Physical*, no. 159, pp. 196-203, 2010.

[44] G. Manla, N. M. White and J. Tudor, "Harvesting energy from vehicle wheels," 15th International Conference on Solid-State Sensors, Actuators and Microsystems. Transducers, p. 1389–1392, 2009.

[45] Y. Hu, C. Xu, Y. Zhang, L. Lin and R. L. W. Z. L. Snyder, "A nanogenerator for energy harvesting from a rotating tire and its application as a self-powered pressure/speed sensor," *Advanced Materials*, vol. 23, pp. 4068-4071, 2011.

[46] F. Khameneifar, M. Moallem and S. Arzanpour, "Modeling and analysis of a piezoelectric energy scavenger for rotary motion applications," *Journal of Vibration and Acoustics*, vol. 133, 2011.

[47] L. Gu and C. Livermore, "Passive self-turning energy harvester for extracting energy from rotational motion," *Applied Physics Letters*, vol. 97, 2010.

[48] J. Cannarella, J. Selvaggi, S. Salon, J. Tichy and D.-A. Borca-Tasciuc, "Coupling factor between the magnetic and mechanical energy domains in electromagnetic power harvesting applications," *IEEE Transactions of Magnetics*, vol. 47, no. 8, pp. 2076-2080, 2011.

[49] V. Bedekar, J. Oliver and S. Priya, "Pen harvester for powering a pulse rate sensor," *Journal of Physics D: Applied Physics*, vol. 42, 2009.

[50] J. Liu and S. Garrett, "Characterization of a small moving-magnet electrodynamic linear motor," *Journal of the Acoustical Society of America*, vol. 118, no. 4, p. 2289–2294, 2005.

[51] D. Spreemann, D. Hoffmann, B. Folkmer and Y. Manoli, "Numerical optimization approach for resonant electromagnetic vibration transducer designed for random vibration," *Journal of Micromechanics and Microengineering*, vol. 18, 2008.

[52] B. Delinchant, F. Wurtz, J.-P. Yonnet and J.-L. Coulomb, "Interaction between ring-shaped permanent magnets with symbolic gradients: application to magnetic bearing system optimization," *IEEE Transactions on Magnetics*, vol. 47, no. 5, pp. 1418-1421, 2011.

[53] P. Wang, K. Tanaka, S. Sugiyama, X. Dai, X. Zhao and J. Liu, "A micro electromagnetic low level vibration energy harvester based on MEMS technology," *Microsystem Technologies*, vol. 15, pp. 941-951, 2009.

[54] A. J. Sneller and B. P. Mann, "On the nonlinear electromagnetic coupling between a coil and an oscillating magnet," *Journal of Physics D: Applied Physics*, vol. 43, 2010.

[55] G. Donoso, C. L. Ladera and P. Martín, "Magnet fall inside a conductive pipe: motion and the role of the pipe wall thickness," *European Journal of Physics*, vol. 30, pp. 855-869, 2009.

[56] Magcraft, *Permanent Magnet Selection and Design Handbook*, Vienna, VA, 2007.

[57] D. Zhu, S. Roberts, M. J. Tudor and S. P. Beeby, "Design and experimental characterization of a tunable vibration-based electromagnetic micro-generator," *Sensors and Actuators A: Physical*, 2010.

[58] H. A. Wheeler, "Simple inductance formulas for radio coils," in Proceedings of the Institute of Radio Engineers, 1928.

[59] National Institute of Standards and Technology, Copper wire tables, 1966.

[60] WebElements, "Electrical Resistivity," http://www.webelements.com/periodicity/electrical_resistivity/.

[61] Prüftechnik, *Reducing vibration by balancing rotor blades*, 2009.

[62] IRD Balancing, *Balance quality requirements of rigid rotors*, 2009.

[63] K. Chintalapudi, J. Paek, N. Kothari, S. Rangwala, R. Govindan and E. Johnson, "Embedded sensing of structures: a reality check," in 11th IEEE International Conference on Embedded and Real-Time Computing Systems and Applications, Hong Kong, 2005.

[64] B. L. Grisso, J. Kim, J. R. Farmer, D. S. Ha and D. J. Inman, "Thermal energy harvested to power digital SHM hardware," in Virginia Space Grant Consortium, Norfolk, VA, 2008.

Appendix A: MATLAB Code

The MATLAB code is broken into several subprograms. A "driver" program executes the subprograms and plots the results. The driver first calls another script file which creates the default parameters and inputs to the model. Different files can be created for different sets of common parameters. Next the driver can allow the user to change any of these parameters, choose which model to use (standard model from Chapter 2 or the model without the harvester coil), and choose which circuit to use (load resistor circuit, simple energy storage circuit, or load resistor circuit without the coil inductance). Next the appropriate model function is called to simulate the harvester. Within the model function, the energy storage circuit code may be called if requested. With the time response of the system computed, the driver code computes other parameters from the computer variables and plots the results.

Driver Program

```
%% ===== HARIE ====
% This function determines the mechanical and the electrical results
% of the rotating electromagnetic energy harvester.
%
% -- Simulation Type --
% - Model -
% Model = 1: Full model of the harvester
% Model = 2: Model which ignores the presence of the coil
%
% - Circuit -
% Circuit = 1: Load resistor circuit
% Circuit = 2: Simple energy storage circuit
% Circuit = 3: Load resistor circuit ignoring coil inductance
%
%
% -- Major Variables --
% theta = angle of the harvester tube with respect to vertically up
%   position, radians
% r = radial distance of slider, meters
% r_t = dr/dt = time rate of change of r, m/s
% EMF = epsilon = induced voltage in the coil, Volts
% I = current through the coil, A
% IC = current through the capacitor, A
```

```
% VC = voltage across the capacitor, Volts
%
% Note: All units are metric unless otherwise stated.

clc; clear; close all


%% ===== Inputs =====
% -- Default Inputs --
Inputs_Rotating_PrototypeHarvester;

% -- Simulation Type --
Model = 1;
Circuit = 3;

% -- Frequently Varied Parameters --
OmegaMagRPM = 10;
Omega = @(t) OmegaMagRPM*2*pi/60;

cycles = 1;
T = cycles/(OmegaMagRPM/60);

inches = 0.0254;    % = 1 leaves distances in m; = 0.0254 converts to in


%% ===== Solve Equations =====
switch Model
    case 1
% - Model 1: Fully Coupled Solution -
   [t,theta,r,r_t,I,IC,VC,alpha] = HARIE_Model1(Omega, ...
        theta0,r0,r_t0, I0, VC0, ...
        T, dt, ...
        r1, r2, ...
        c1, c2, a1, a2, lV, ...
        m, M, ...
        mus, muk, g, ...
        Circuit, Rcoil, Lcoil, Vbridge, C, Rload);
    case 2
% - Model 2: No Coil Inductance -
   [t,theta,r,r_t,I,IC,VC,alpha] = HARIE_Model2(Omega, ...
        theta0,r0,r_t0, I0, VC0, ...
        T, dt, ...
        r1, r2, ...
        c1, c2, a1, a2, lV, ...
        m, M, ...
        mus, muk, g, ...
        Circuit, Rcoil, Lcoil, Vbridge, C, Rload);
    case 3
% - Model 3: No Coil -
   [t,theta,r,r_t,I,IC,VC,alpha] = HARIE_Model3(Omega, ...
        theta0,r0,r_t0, I0, VC0, ...
        T, dt, ...
        r1, r2, ...
        c1, c2, a1, a2, lV, ...
        m, M, ...
        mus, muk, g, ...
        Rcoil, Rload);
end

% - Convert meters to inches -
r = r/inches;
c1 = c1/inches; c2 = c2/inches;
r1 = r1/inches; r2 = r2/inches;

Vload = I*Rload;
Pload = I.^2*Rload;
Eload = trapz(t,Pload);
Pload_avg = Eload/T*1000;    % Average Load Power in mW
disp(['Average Load Power = ',num2str(Pload_avg,'%4.4f'),' mW'])

EMF = alpha.*r_t;
```

```
%% ===== Plot Results =====
%% - Mechanics and EMF
figure(1);
% - Subplot: theta v. Time -
subplot(3,2,1); hold on; grid
plot(t,mod(theta,2*pi),'k','linewidth',2);
ylim([0 2*pi])
xlabel('Time t, s','fontsize',12)
ylabel('Harvester Angle \theta, rad','fontsize',12)

% - Subplot: r_t vs. Time -
subplot(3,2,5); hold on; grid
plot(t,r_t,'g','linewidth',2);
xlabel('Time t, s','fontsize',12)
ylabel('dr/dt, m/s','fontsize',12)

% - Subplot: r vs. Time -
subplot(3,2,3); hold on; grid
plot(t,r,'b','linewidth',2);
xlabel('Time t, s','fontsize',12)
if inches ~= 0.0254; ylabel('Radial Position r, m','fontsize',12);
else ylabel('Radial Position r, in','fontsize',12); end
plot([0,T],[c1,c1],'c','linewidth',2)
plot([0,T],[c2,c2],'c','linewidth',2)

% - Subplot: Induced Voltage vs. Time -
subplot(3,2,2); hold on; grid
plot(t,EMF,'r','linewidth',2)
xlabel('Time t, s','fontsize',12)
ylabel('Induced Voltage \epsilon, V','fontsize',12)

%% - Electrical Results
figure(1);

if Circuit ~= 2;

% - Subplot: Current vs. Time -
subplot(3,2,4); hold on; grid
plot(t,I,'m','linewidth',2);
xlabel('Time t, s','fontsize',12)
ylabel('Current I, A','fontsize',12)

% - Subplot: Load Power vs. Time -
subplot(3,2,6); hold on; grid
plot(t,Pload*1000,'g','linewidth',2)
plot([0 T],[Pload_avg Pload_avg],'r')
xlabel('Time t, s','fontsize',12)
ylabel('Load Power P_L, mW','fontsize',12)

else

% - Subplot: Current -
subplot(3,2,4); hold on; grid
plot(t,I,'b','linewidth',2)
plot(t,IC,'g','linewidth',2)
xlabel('Time t, s','fontsize',12)
ylabel('Current I, A','fontsize',12)
legend('I','I_C','Location','SouthEast')

% - Subplot: Capacitor Voltage -
subplot(3,2,6); hold on; grid
plot(t,VC,'linewidth',2)
xlabel('Time t, s','fontsize',12)
ylabel('Capacitor Voltage, V_C','fontsize',12)

end

%% - Orbit
figure(2); hold on; axis equal
```

```
CircleAngle = linspace(0,2*pi,100);

% - Tube Limits -
[x,y] = pol2cart(CircleAngle,r1*ones(1,100)); plot(x,y,'r')
[x,y] = pol2cart(CircleAngle,r2*ones(1,100)); plot(x,y,'r')

% - Coil Limits -
[x,y] = pol2cart(CircleAngle,c1*ones(1,100)); plot(x,y,'c')
[x,y] = pol2cart(CircleAngle,c2*ones(1,100)); plot(x,y,'c')

% - Plot Magnet's Path -
x = r.*sin(theta); y = r.*cos(theta);
plot(x,y,'linewidth',2); axis equal
% plot(x(1),y(1),'ro','MarkerFaceColor','r', ...
%      'markersize',5,'linewidth',2)
if inches ~= 0.0254; xlabel('meters','fontsize',12); ylabel('meters','fontsize',12);
else xlabel('inches','fontsize',12); ylabel('inches','fontsize',12); end
```

Default Inputs

```
%% ==== Inputs_Rotating_PrototypeHarvester ===
% This code loads the parameters for the rotating prototype harvester.

%% -- Driving Rotation: Omega = d(theta)/dt --
OmegaMagRPM = 15;    % OmegaMagRPM = magnitude
                     %   of rotor speed in RPM
Omega = @(t) OmegaMagRPM*2*pi/60;    % Omega = rotor speed in rad/s

%% -- Simulation Parameters --
dt = 0.0001;         % dt = time step, s
cycles = 1;          % cycles = number of cycles to perform
T = cycles/OmegaMagRPM*60;    % T = run time, s

%% -- System Parameters --
% - Dynamic Constants -
g = 9.81;            % g = acceleration due to gravity, m/s^2
muk = 0.25;          % muk = kinetic coefficient of friction
mus = 0.35;          % mus = static coefficient of friction

% - Slider Tube -
r1 = (1.875+0.25)*0.0254;    % r1 = minimum allowable radius, m
r2 = (9.25-0.25)*0.0254;     % r2 = maximum allowable radius, m
rs = (r1+r2)/2;              % rs = center of tube radius, m

% - Coil -
c1 = (4.625)*0.0254;         % c1 = minimum coil position, m
c2 = (4.625+1.19)*0.0254;    % c2 = maximum coil position, m
a1 = (1.0180)/2*0.0254;      % a1 = inner radius of coil, m
a2 = (2.0150)/2*0.0254;      % a2 = outer radius of coil, m

Rcoil = 426;         % Rcoil = resistance of coil, ohms
Lcoil = 0.998;       % Lcoil = inductance of coil, Henrys

lw = Rcoil/(0.538248);              % lw = length of wire for AWG 32, m
lV = lw/(pi*(a2^2-a1^2)*(c2-c1));   % lV = lw/Vcoil

FF = lw*pi*(0.0002032/2)^2/(pi*(a2^2-a1^2)*(c2-c1)); % FF = Coil fill
                                                     %      factor

% - Magnet -
M = 0.018;           % M = mass of magnet, kg
m = 2.1;             % m = magnetic dipole moment, A-m^2
```

```
% - Circuit -
Rload = 176.1;      % Rload = Resistance in the output circuit, ohms
Vbridge = 0.6;      % Vbridge = voltage drop across rectifier bridge, Volts
C = 1;              % C = capacitance of capacitor, Farads

%% -- Initial Conditions --
theta0 = pi;        % theta0 = theta(t=0)
r0 = r2;            % r0 = r(t=0)
r_t0 = 0;           % r_t0 = dr/dt(t=0)
I0 = 0;             % I0 =  I(t=0)
VC0 = 0;            % VC0 = VC(t=0)
```

Model Solvers

Model 1: Primary Solver

```
function [t,theta,r,r_t,I,IC,VC,alpha] = HARIE_Model1(Omega, ...
        theta0,r0,r_t0, I0, VC0, ...
        T, dt, ...
        r1, r2, ...
        c1, c2, a1, a2, lV, ...
        m, M, ...
        mus, muk, g, ...
        Circuit, Rcoil, Lcoil, Vbridge, C, Rload)

% This function solves the governing equations of the energy harvester.
% It solves the mechanical and electrical equations simultaneously and
% includes the coil inductance term.  This is the primary numerical solver.

% Note: Y = [theta; r; r_t]

t = 0:dt:T; t=t';
Y = zeros(length(t),3);
EMF = zeros(length(t),1);
I = EMF; IC = EMF; VC = EMF; alpha = EMF;

Y(1,:) = [theta0,r0,r_t0];
alpha(1) = Alpha_Function(r0, m, lV, c1, c2, a1, a2);
I(1) = I0;
IC(1) = abs(I0);
VC(1) = VC0;

for i=2:length(t)
%% ===== Mechanics with Friction =====
ap = Y(i-1,2)*Omega(i-1)^2 - g*cos(Y(i-1,1)) - alpha(i-1)/M*I(i-1);
an = g*sin(Y(i-1,1)) - 2*Y(i-1,3)*Omega(i-1);

dYdt = [Omega(i-1);
    Y(i-1,3);
    ap-muk*abs(an)*sign(Y(i-1,3))];
Y(i,:) = dYdt'*dt + Y(i-1,:);

if (Y(i,2) >= r2) && (Y(i,3) > 0)       % Top of slider tube
    Y(i,2) = r2;
    Y(i,3) = 0;
elseif (Y(i,2) <= r1) && (Y(i,3) < 0)   % Bottom of slider tube
    Y(i,2) = r1;
    Y(i,3) = 0;
elseif abs(ap) < mus*abs(an) && Y(i-1,3) == 0
```

```
    Y(i,2) = Y(i-1,2);
    Y(i,3) = 0;
end


%% ===== Circuitry =====
alpha(i)=Alpha_Function(Y(i,2),m,lV,c1,c2,a1,a2);
switch Circuit
    case 1
        I(i,1) = 1/Lcoil*(alpha(i)*Y(i,3)-(Rcoil+Rload)*I(i-1,1))*dt+I(i-1,1);
    case 2
        [I(i,1),IC(i,1),VC(i,1)] = HARIE_Circuit2(dt, alpha(i)*Y(i,3), ...
            Rcoil, Lcoil, Vbridge, C, ...
            IC(i-1,1), VC(i-1,1));
    case 3
        I(i,1) = alpha(i)*Y(i,3)/(Rcoil+Rload);
end

end

%% ===== Assigning Variables =====
theta = Y(:,1);
r = Y(:,2);
r_t = Y(:,3);
clear Y
```

Model 2: Model without Harvester Coil

```
function [t,theta,r,r_t,I,IC,VC,alpha] = HARIE_Model2(Omega, ...
        theta0,r0,r_t0, I0, VC0, ...
        T, dt, ...
        r1, r2, ...
        c1, c2, a1, a2, lV, ...
        m, M, ...
        mus, muk, g, ...
        Rcoil, Rload)
% This function solves the governing equations of the rotating magnet-coil
% assembly.  It uses a semi-coupled solution which ignores the coil
% inductance and drag force from circuit.  It assumes a simple load
% resistor circuit without the coil inductance to compute "power".

% Note: Y = [theta; r; r_t]

t = 0:dt:T; t=t';
Y = zeros(length(t),3);
EMF = zeros(length(t),1);
alpha = EMF; IC = EMF; VC = EMF;

Y(1,:) = [theta0,r0,r_t0];
alpha(1) = Alpha_Function(r0, m, lV, c1, c2, a1, a2);

for i=2:length(t)
%% ===== Mechanics With Friction =====
ap = Y(i-1,2)*Omega(i-1)^2 - g*cos(Y(i-1,1));
an = g*sin(Y(i-1,1))-2*Y(i-1,3)*Omega(i-1);

dYdt = [Omega(i-1);
    Y(i-1,3);
    ap-muk*abs(an)*sign(Y(i-1,3))];
Y(i,:) = dYdt'*dt + Y(i-1,:);

if (Y(i,2) <= r1) && (Y(i,3) < 0)    % Bottom of slider tube
    Y(i,2) = r1;
    Y(i,3) = 0;
```

```
    an = g*sin(Y(i-1,1));
elseif (Y(i,2) >= r2) && (Y(i,3) > 0)    % Top of slider tube
    Y(i,2) = r2;
    Y(i,3) = 0;
    an = g*sin(Y(i-1,1));
end

if abs(ap) < mus*abs(an) && Y(i-1,3) == 0 %(Y(i-1,2) == r1 || Y(i-1,2) == r2)
    Y(i,1) = Omega(i-1)*dt + Y(i-1,1);
    Y(i,2) = Y(i-1,2);
    Y(i,3) = 0;
end

alpha(i)=Alpha_Function(Y(i,2),m,lV,c1,c2,a1,a2);

end

I = alpha.*Y(:,3)/(Rcoil+Rload);

%% ===== Assigning Variables =====
theta = Y(:,1);
r = Y(:,2);
r_t = Y(:,3);
clear Y
```

Supporting Functions

Alpha Function

```
function [alpha] = Alpha_Function(r, m, lV, c1, c2, a1, a2)
% This function computes the coupling coefficient between a coil and a
% moving magnetic dipole.
%
% Syntax: [alpha] = Alpha_Function(r, m, lV, c1, c2, a1, a2)
% Inputs:   r = radial distance of slider, meters
%           m = magnetic dipole moment, A*m^2
%           lV = lw/Vcoil; lw = length of wire, m; Vcoil = coil volume, m^3
%           c1 = minimum coil position, m
%           c2 = maximum coil position, m
%           a1 = inner coil radius
%           a2 = outer coil radius
% Outputs:  alpha = coupling coefficient, Volts-s/m

mu0 = 1.2566*10^-6;     % mu0 = permeability constant for free space,
                        %   N*A^-2 or H/m

f1 = @(a,c) a*(a^2+(r-c).^2).^(-1/2)-log(sqrt(a^2+(r-c).^2)+a);
alpha = mu0*lV*m*0.5.*(f1(a2,c2)-f1(a2,c1)-f1(a1,c2)+f1(a1,c1));
```

Simple Energy Storage Circuit

```
function [I,IC,VC] = HARIE_Circuit2(dt, EMF, ...
            Rcoil, Lcoil, Vbridge, C, ...
            IC0, VC0)
% This function computes the currents and voltages associated
% with the simple energy storage circuit.

q0 = C*VC0;
Q0 = [q0;IC0];

if EMF > VC0 + Vbridge
    dQdt =[ IC0;
            1/Lcoil*(EMF-Vbridge-Rcoil*IC0-1/C*q0)];
    Q = dQdt*dt+Q0;
    IC = Q(2,1);
    I = IC;
    VC = Q(1,1)/C;
elseif EMF < -(VC0 + Vbridge)
    dQdt =[ IC0;
            1/Lcoil * (-EMF(1)-Vbridge-Rcoil*IC0-1/C*q0)];
    Q = dQdt*dt+Q0;
    IC = Q(2,1);
    I = -IC;
    VC = Q(1,1)/C;
else
    I = 0;
    IC = 0;
    VC = VC0;
end
```

Appendix B: Free Fall Test Data

Each figure in this appendix plots the voltage across a load resistor versus time. The figures show the measured voltage and model predictions with a magnet dipole moment of 2.21 A-m^2 and with a magnetic dipole moment of 2.1 A-m^2. Five tests were conducted at load resistance. Some of the curves display an "overshoot" when the voltage returns to zero after the magnet has passed through the coil. When the magnet reaches the end of the tube, it impacts a thin foam stopper at the end and recoils slightly. This produces a small amount of voltage (the overshoot in the graphs). This effect adds negligible amounts of energy to the average energy calculation in Equation 2.40.

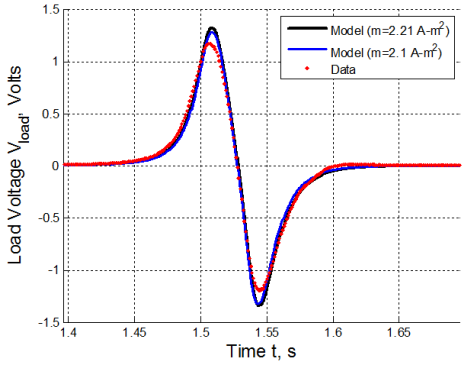

Figure B.1. Load voltage versus time for R_{load} = 51 Ω.

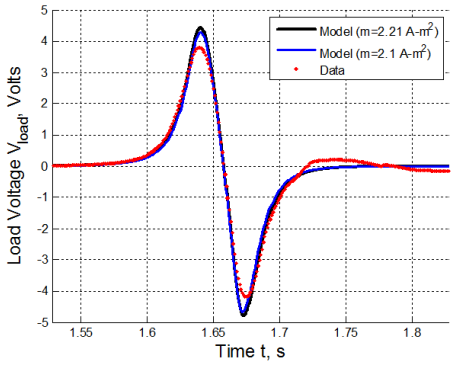

Figure B.2. Load voltage versus time for R_{load} = 220 Ω.

r

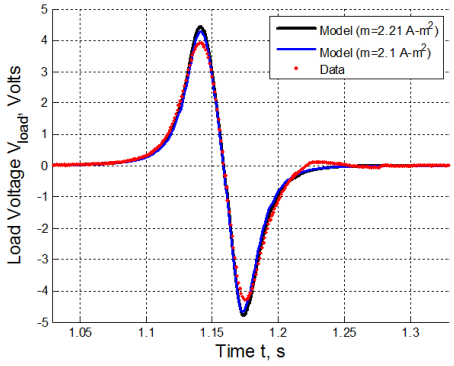

Figure B.3. Load voltage versus time for R_{load} = 384 Ω.

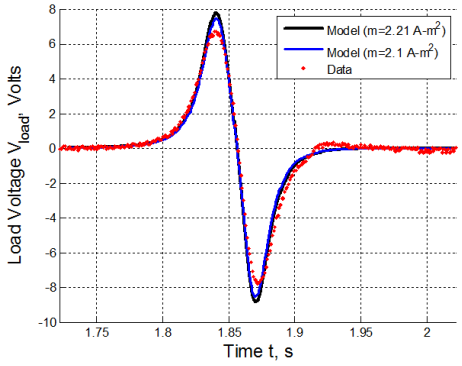

Figure B.4. Load voltage versus time for R_{load} = 555 Ω.

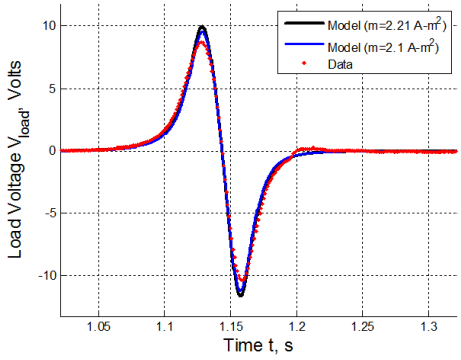

Figure B.5. Load voltage versus time for R_{load} = 1000 Ω.

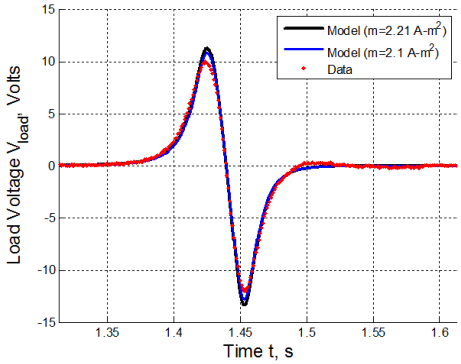

Figure B.6. Load voltage versus time for R_{load} = 1500 Ω.

Appendix C: Rotating Test Data

This appendix presents the load voltage versus time data from the rotating prototype in Section 3.2. In each figure, the first plot shows the voltage over the full 60 second test and the second plot shows a few voltage spikes from that test data.

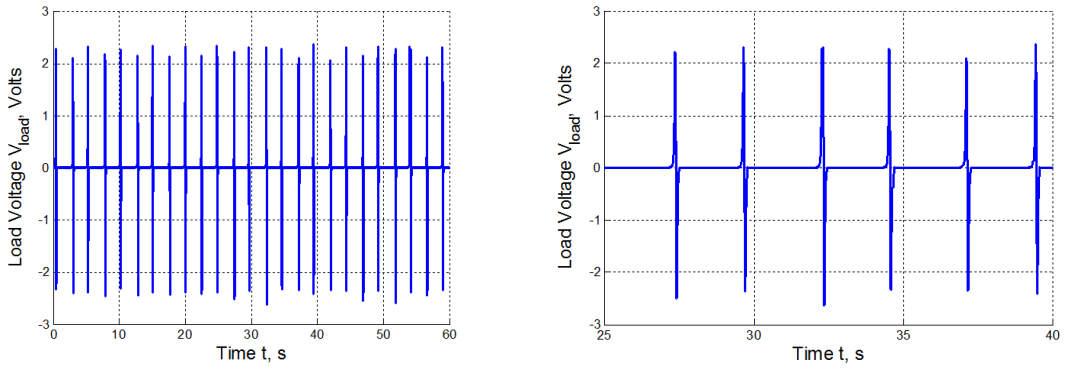

(a) (b)

Figure C.1. Load voltage versus time at 12 RPM.

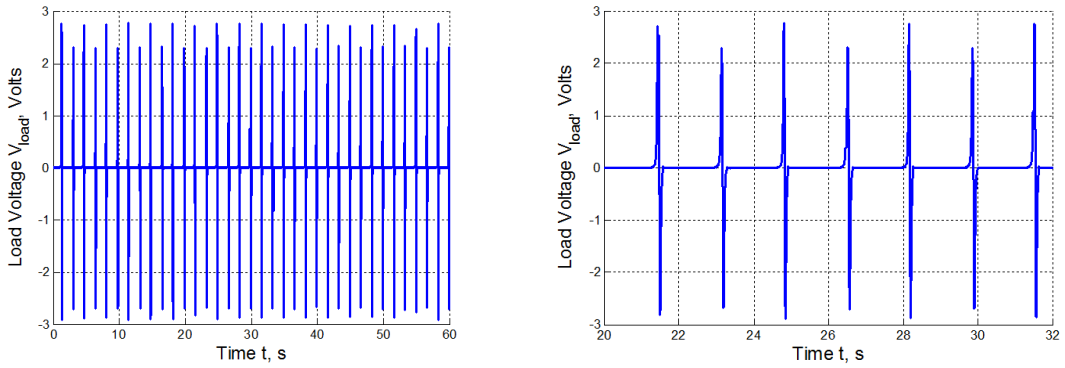

(a) (b)

Figure C.2. Load voltage versus time at 18 RPM.

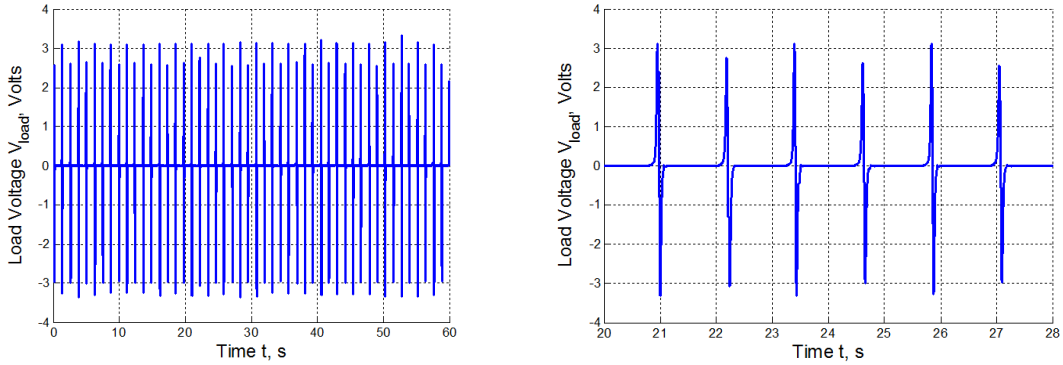

(a) (b)

Figure C.3. Load voltage versus time at 25 RPM.

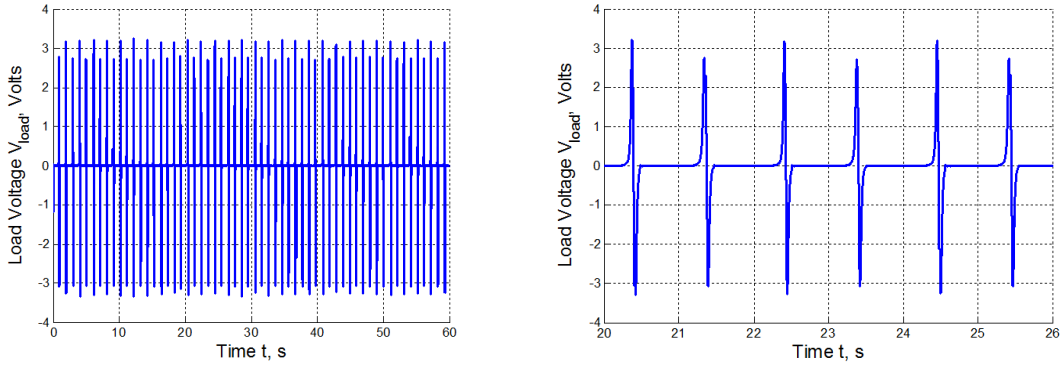

(a) (b)

Figure C.4. Load voltage versus time at 29 RPM.

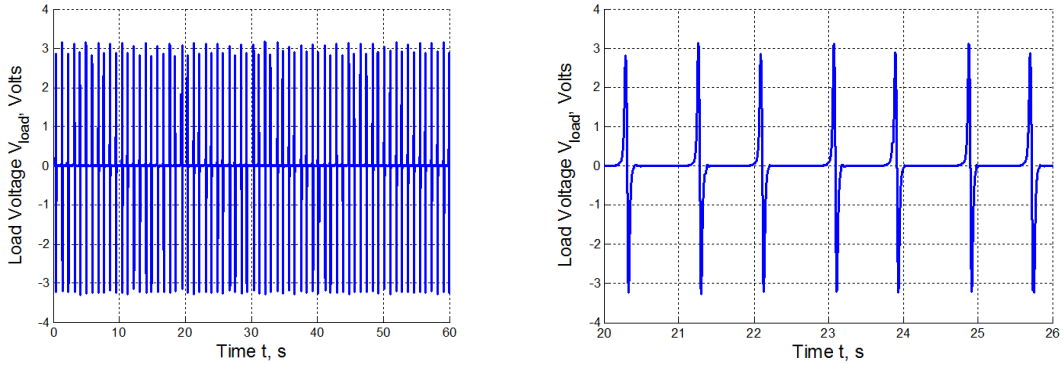

(a) (b)

Figure C.5. Load voltage versus time at 33 RPM.

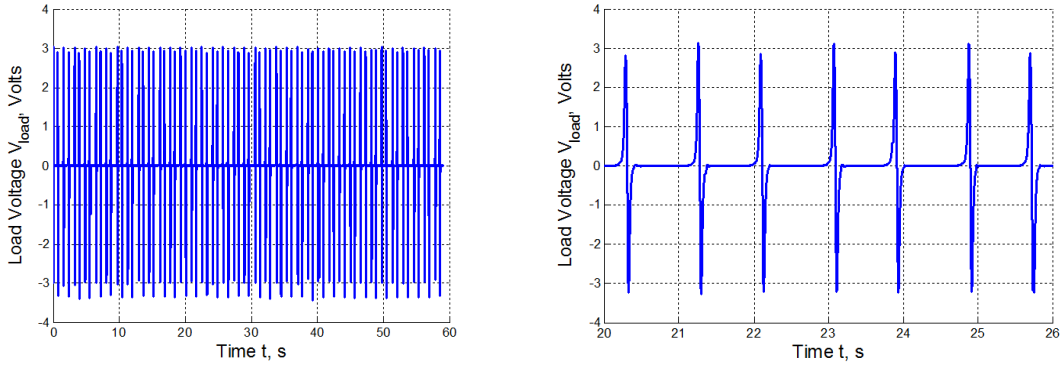

(a) (b)

Figure C.6. Load voltage versus time at 37 RPM.

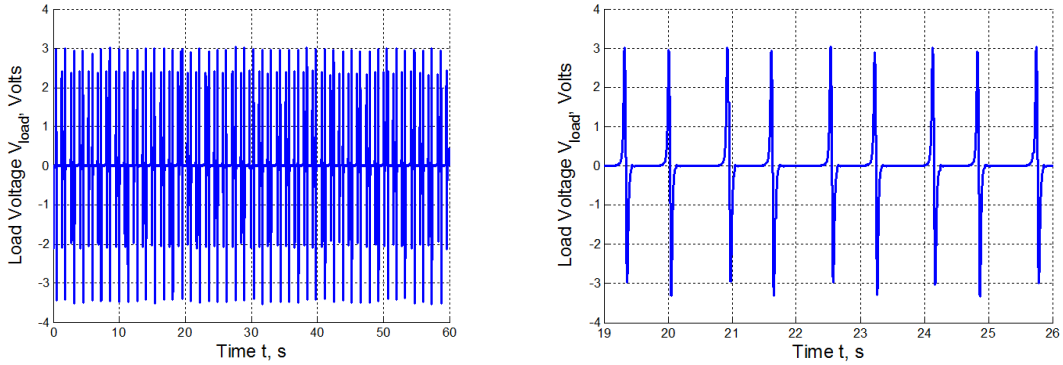

(a) (b)

Figure C.7. Load voltage versus time at 44 RPM.

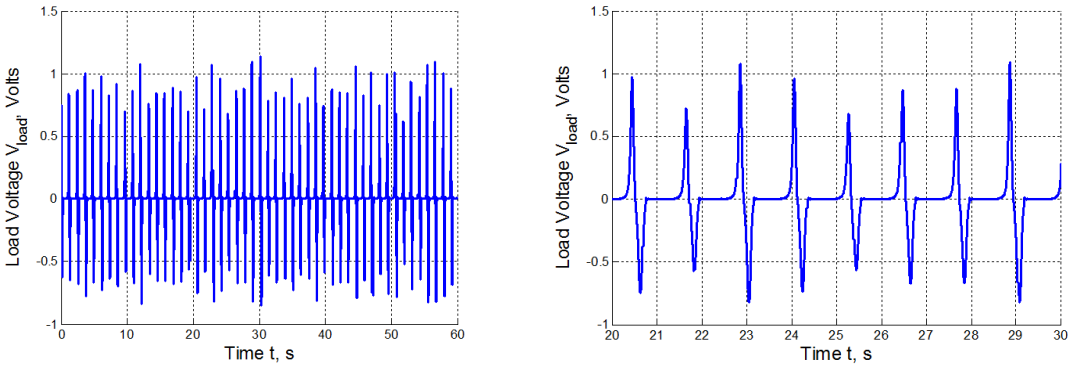

(a) (b)

Figure C.8. Load voltage versus time at 50 RPM.

Appendix D: Capacitor Charging Test Data

In addition to charging the 0.1 F capacitor in Section 3.3, other capacitors were tested. Table D.1 lists the capacitors tested and the rotation speeds at which they were tested. The goal was to test each capacitor at 15 RPM as this is a speed one would expect to see in a full scale wind turbine. However there was some difficulty in precisely setting the rotation speed of the rotating test wheel. Figure D.1 below plots the voltage across the capacitor versus time and the energy versus time for each case. Based on the stored energy graph in Figure D.1, the 0.1 F test was the best performing and was thus represented in Section 3.3. The wireless DAQ could only measure voltages between -10 V and 10 V, thus the voltage for the 470 μF was clipped.

Table D.1. Capacitors tested and their rotation speeds.

Capacitor	Rotation Rate
470 μF	15 RPM
1000 μF	15 RPM
1500 μF	17 RPM
0.1 F	17 RPM
1.0 F	16 RPM

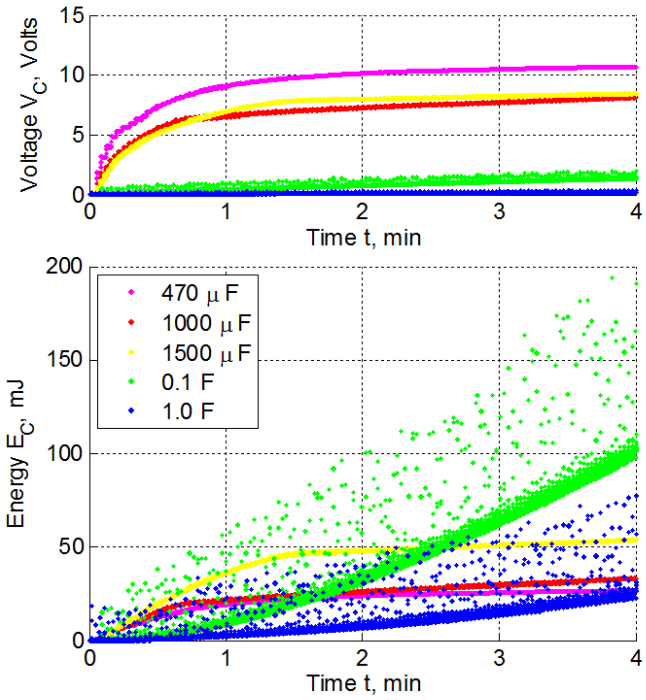

Figure D.1. Capacitor voltage and energy versus time for various capacitors.